Mechanics of plates and shells

Vincent Démery

Gulliver, ESPCI Paris PSL and CNRS, Paris, France

October 24, 2025

Contents

Chapter 1

Mechanics and geometry of plates

1.1 Mechanics

1.1.1 Solid mechanics in three dimensions

Consider a deformation that takes a piece of material from $\boldsymbol{r}$ to $\boldsymbol{R}(\boldsymbol{r}) = \boldsymbol{r} + \boldsymbol{u}(\boldsymbol{r})$, where $\boldsymbol{u}(\boldsymbol{r})$ is the displacement. Assuming that the material is initially at rest, its reference metric is $\bar{g}_{ij} = \delta_{ij}$, where i and j indicate the components of the rank 2 tensor g^0. Now the metric of the deformed material is

$$g_{ij} = \partial_i \boldsymbol{R} \cdot \partial_j \boldsymbol{R}. \tag{1.1}$$

To order one in $\nabla \boldsymbol{u}$, the metric is

$$g_{ij} = \delta_{ij} + \partial_i u_j + \partial_j u_i. \tag{1.2}$$

The strain is defined as the difference with the reference metric:

$$\epsilon_{ij} = \frac{g_{ij} - \bar{g}_{ij}}{2} = \frac{1}{2} \left(\partial_i u_j + \partial_j u_i \right). \tag{1.3}$$

The stress describes the forces in the material. It is also a rank 2 tensor, which we denote σ_{ij}. The force exerted through a surface of a normal $\boldsymbol{n}$ and area δA is given by

$$\delta F_i = \delta A \sigma_{ij} n_j. \tag{1.4}$$

We use Einstein convention for the summation over repeated indices.

The only linear isotropic tensorial relation between the strain and strain tensors is the Hooke's law:

$$\boxed{\sigma_{ij} = \frac{E}{1+v} \left(\epsilon_{ij} + \frac{v}{1-2v} \epsilon_{kk} \delta_{ij} \right),} \tag{1.5}$$

where E is the Young's modulus and v is the Poisson ratio. This relation can be inverted; taking the trace of this relation we get $\sigma_{kk} = \frac{E}{1-2v} \epsilon_{kk}$, and we deduce

$$\boxed{\epsilon_{ij} = \frac{1}{E} \left[(1+v)\sigma_{ij} - v\sigma_{kk}\delta_{ij} \right].} \tag{1.6}$$

From a force balance on a small volume element, we arrive at the equilibrium equation:

$$\boxed{\partial_i \sigma_{ij} = 0.} \tag{1.7}$$

By computing the work of the forces on a small volume element, we find the volumic energy density:

$$\boxed{e = \frac{1}{2} \sigma_{ij} \epsilon_{ij}.} \tag{1.8}$$

1.1.2   Parametrization of a plate, strain

The configuration of the plate is usually described as if it were a purely two-dimensional object. We use internal coordinates $r = (s, t) \in \mathbb{R}^2$, which do not need to match with the Cartesian coordinates, and the shape is described by a function $R(r) \in \mathbb{R}^3$. If the rest shape is described by the function $\bar{R}(r)$, then the metrics $\bar{g}$ and g can be defined as in the previous section and the strain can be defined.

In the simplest situations, the sheet does not depart too much from its flat rest configuration, so that we can use the Cartesian coordinates $r = (x, y)$ for the internal coordinates, the reference configuration is $\bar{R}(x, y) = (x, y, 0)$ and we can write the deformed configuration as

$$R(x, y) = \begin{pmatrix} x + u(x, y) \\ y + v(x, y) \\ w(x, y) \end{pmatrix}. \tag{1.9}$$

The rest and deformed metrics are

$$\bar{g} = \begin{pmatrix} 1 & 0 \\ 0 & 1 \end{pmatrix}, \tag{1.10}$$

and

$$g = \begin{pmatrix} (1 + u_x)^2 + v_x^2 + w_x^2 & (1 + u_x)u_y + v_x(1 + v_y) + w_x w_y \\ (1 + u_x)u_y + v_x(1 + v_y) + w_x w_y & u_y^2 + (1 + v_y)^2 + w_y^2 \end{pmatrix}, \tag{1.11}$$

where we denote the partial derivatives with indices: $\partial_x u = u_x$, etc.

We consider small deformations, and we want to expand to the lowest non trivial order in the displacements u, v and w. We see in the term g_{xx} that the term u_x compares to w_x^2, thus we retain terms of order two in w and one in u. This gives for the strain

$$\boxed{\epsilon = \frac{g - \bar{g}}{2} = \begin{pmatrix} u_x + \frac{w_x^2}{2} & \frac{u_y + v_x + w_x w_y}{2} \\ \frac{u_y + v_x + w_x w_y}{2} & v_y + \frac{w_y^2}{2} \end{pmatrix}.} \tag{1.12}$$

The scaling $u \sim v \sim w^2$ means that the out-of-plane displacement is much larger than the in-plane displacement.

Note that, in some cases, it may be important to keep the quadratic terms u^2 and v^2 in the strain.

1.1.3   Stretching modulus and Poisson ratio

We now consider a plate with thickness t. Because of the free boundaries in the direction perpendicular to the plates, which we choose to be the z direction, the stress should satisfy $\sigma_{iz} = 0$ for $i \in \{x, y, z\}$: this is the *plane stress condition*.

Due to Hooke's law, $\epsilon_{iz} = 0$ for $i \in \{x, y\}$ and, using the plane stress condition in Hooke's law (Eq. (1.5), we get

$$0 = (1 - 2v)\epsilon_{zz} + v\epsilon_{kk} = (1 - v)\epsilon_{zz} + v\epsilon_{kk}^{(2)}, \tag{1.13}$$

where the superscript (2) refers to the two-dimensional strain along the sheet. As a consequence, we have

$$\epsilon_{kk} = \epsilon_{kk}^{(2)} + \epsilon_{zz} = \frac{1 - 2v}{1 - v}\epsilon_{kk}^{(2)}, \tag{1.14}$$

which can be inserted in the Hooke's law:

$$\sigma_{ij} = \frac{E}{1 + v}\left(\epsilon_{ij} + \frac{v}{1 - v}\epsilon_{kk}^{(2)}\delta_{ij}\right). \tag{1.15}$$
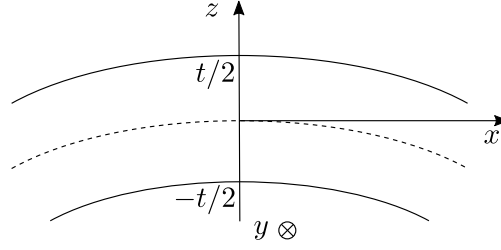
Figure 1.1: Plate bent in around the direction y.

Finally, we are interested in forces integrated over the thickness of the sheet, which leads us to define the in-plane stress

$$\sigma_{ij}^{(2)} = t\sigma_{ij} = \frac{Y}{1+\nu}\left(\epsilon_{ij}^{(2)} + \frac{\nu}{1-\nu}\epsilon_{kk}^{(2)}\delta_{ij}\right),$$

(1.16)

where we have introduced the *stretching modulus*

$$Y = Et.$$

(1.17)

Note that the stress of solid mechanics has the dimension of a pressure, energy/length^3, while the planar stress in sheets has the dimension of a line tension, or surface energy, energy/length^2.

1.1.4 Bending

Plates also resist bending. We consider a plate bent in the (x, y) plane with a radius of curvature R (Fig. 1.1).

At $x = 0$, the height $z = 0$ corresponds to the middle of the plate; the elongation due to the bending is thus

$$\epsilon_{xx} = z/R,$$

(1.18)

for $z \in [-t/2, t/2]$. We use the plane stress condition, $\sigma_{iz} = 0$. Along the direction y, it can be shown that a no stress condition can lead to large strains, so that we use $\epsilon_{yy} = 0$ instead. Using Eq. (1.13), we can deduce that the stress in the x direction is given by

$$\sigma_{xx} = \frac{E}{1-\nu^2}\epsilon_{xx}.$$

(1.19)

Integrating the volumic energy density over the thickness, we get

$$\int_{-t/2}^{t/2} \frac{1}{2}\sigma_{xx}\epsilon_{xx}\mathrm{d}z = \frac{E}{2(1-\nu^2)R^2}\int_{-t/2}^{t/2} z^2\mathrm{d}z = \frac{B}{2R^2},$$

(1.20)

where we have introduced the *bending modulus*

$$B = \frac{Et^3}{12(1-\nu^2)}.$$

(1.21)

We can also compute the moment along y exerted by the part $x > 0$ on the part $x < 0$:

$$M = \int_{-t/2}^{t/2} z\sigma_{xx}\mathrm{d}z = \frac{B}{R}.$$

(1.22)

1.1.5 Föppl-von Kármán equations

The in-plane force balance is analogous to the 3d force balance:

$$\partial_i \sigma_{ij} = 0. \tag{1.23}$$

For the out-of-plane force balance, a direct derivation is cumbersome [Audoly and Pomeau, 2010, Secs. 6.4 and 6.5] so we resort to a one-dimensional derivation, which can be used for a rod, that we generalize to a plate.

We denote $w(x, y)$ the height of the plate at the position (x, y); in the first step, we assume that it depends only on x. The moment exerted through a section at x (from the part on the right to the part on the left) has been computed above (Eq. (1.22)):

$$M(x) = \frac{B}{R(x)} = -Bw''(x), \tag{1.24}$$

where the primes denote derivatives and the minus sign comes from the fact that $w''(x) < 0$ in Fig. 1.1.

The force along x exerted through this section is $\sigma_{xx}(x)$, where σ_{ij} is now a two-dimensional stress. We now perform a momentum balance on the part of the sheet located between x and $x + \delta x$. Expressing the momenta at x, it reads

$$-M(x) + M(x + \delta x) + w'(x)\delta x \times \sigma_{xx}(x) = 0. \tag{1.25}$$

Taking the limit $\delta x \to 0$, we have

$$Bw''' - \sigma_{xx}w = 0. \tag{1.26}$$

Deriving, we arrive at

$$B\partial_x^4 w = \partial_x(\sigma_{xx}\partial_x w). \tag{1.27}$$

The two-dimensional generalization is

$$B\nabla^4 w = \partial_i(\sigma_{ij}\partial_j w), \tag{1.28}$$

where $\nabla^4 = (\partial_x^2 + \partial_y^2)^2$. The derivative on the right hand side can be developped, and using the in-plane force balance we get $\partial_i(\sigma_{ij}\partial_j w) = \sigma_{ij}\partial_i\partial_j w$.

Finally, we obtain the Föppl-von Kármán equations:

$$\partial_i \sigma_{ij} = 0, \tag{1.29}$$

$$B\nabla^4 w - \sigma_{ij}\partial_i\partial_j w = 0. \tag{1.30}$$

External forces can be added in these equations. For instance, if a pressure P is applied below the plate the out-of-plane equation becomes

$$B\nabla^4 w - \sigma_{ij}\partial_i\partial_j w = P. \tag{1.31}$$

Note that without the bending modulus, this equation is a generalization of the Laplace law, $-\gamma\nabla^2 w = P$.

The Föppl-von Kármán equations can be derived from the elastic energy that contains stretching and bending contributions. However, the exact form of the energy is not straightforward [Audoly and Pomeau, 2010, Sec. 6.6].

1.1.6 Covariant formulation

We have given above the Föppl-von Kármán equations for small deviations to a flat configuration. However, when there are large deviations to a flat configuration, one has to use a covariant expression of these equations [Dias et al., 2011].

The second derivatives of the height, $\partial_i \partial_j w$, is replaced by the curvature tensor

$$c_{ij} = \hat{\boldsymbol{n}} \cdot \partial_i \partial_j \boldsymbol{R}, \tag{1.32}$$

where $\hat{\boldsymbol{n}}$ is the unit vector normal to the surface; it may be constructed by normalizing $\partial_1 \boldsymbol{R} \times \partial_2 \boldsymbol{R}$. In the covariant formulation, the covariant or contravariant nature of the indices matters, and the metric g_{ij} or its inverse, g^{ij} has to be used to raise or lower the indices; for instance $c^{ij} = g^{ik} g^{jl} c_{kl}$. From the curvature tensor, we define the mean curvature H and the Gaussian curvature K:

$$H = \frac{1}{2} c_i^i = \frac{1}{2} \operatorname{Tr}(c_j^i), \tag{1.33}$$

$$K = \frac{1}{2}(c_i^i c_j^j - c_i^j c_j^i) = c_1^1 c_2^2 - c_1^2 c_2^1 = \det(c_j^i). \tag{1.34}$$

The derivatives need to be replaced by covariant derivatives, which involve the Christoffel symbols

$$\Gamma_{jk}^i = \frac{1}{2} g^{il} \left(\partial_j g_{kl} + \partial_k g_{jl} - \partial_l g_{jk} \right). \tag{1.35}$$

The covariant derivative D_i of a tensor a of rank n contains n Christoffel symbols:

$$D_i a^{jk\cdots} = \partial_i a^{jk\cdots} + \Gamma_{il}^j a^{lk} + \Gamma_{il}^k a^{jl} + \cdots \tag{1.36}$$

With these definitions, we can give the covariant Föppl-von Kármán equations:

$$D_i \sigma^{ij} = 0, \tag{1.37}$$

$$c_{ij} \sigma^{ij} = 2B \left[D_i D^i H + 2H(H^2 - K) \right]. \tag{1.38}$$

This formalism has proven useful to compute the stress in a stretched and twisted ribbon [Chopin et al., 2015]: the coupling between the longitudinal stress and the curvature generates a longitudinal stress, which can lead to the transverse buckling of the ribbon.

Polar coordinates. The covariant equations also provide an elegant way to deal with polar coordinates. We consider a planar plate parametrized with the polar coordinates (r, θ); this parametrization is often used in axisymmetric configurations. The rest shape is thus given by

$$\boldsymbol{R}(r, \theta) = \begin{pmatrix} r \cos(\theta) \\ r \sin(\theta) \\ 0 \end{pmatrix}, \tag{1.39}$$

and the associated metric is

$$(g_{ij}) = \begin{pmatrix} 1 & 0 \\ 0 & r^2 \end{pmatrix}. \tag{1.40}$$

The only non-zero derivative appearing in the Christoffel symbols (Eq. (1.35)) is $\partial_r g_{\theta\theta}$. As a consequence, the only non-zero Christoffel symbols are

$$\Gamma_{\theta\theta}^r = -r, \tag{1.41}$$

$$\Gamma_{r\theta}^\theta = 1/r. \tag{1.42}$$

Note that the symbols Γ^i_{jk} are symmetric under the exchange $j \leftrightarrow k$.

We now use the covariant formalism to write down the in-plane force balance (1.37):

$$0 = D_i \sigma^i_j \tag{1.43}$$

$$= \partial_i \sigma^i_j + \Gamma^i_{im} \sigma^m_j - \Gamma^m_{ij} \sigma^i_m. \tag{1.44}$$

In the radial direction, $j = r$, we get

$$\partial_r \sigma^r_r + \frac{1}{r} \left(\sigma^r_r - \sigma^\theta_\theta \right) = 0. \tag{1.45}$$

We have assumed for simplicity that there is no shear stress, $\sigma^\theta_r = 0$. Rearranging, we get

$$\partial_r (r \sigma^r_r) = \sigma^\theta_\theta. \tag{1.46}$$

This expression can also be obtained by computing the radial force on a small piece of plate. The mixed coordinates (covariant and contravariant) for the stress are the ones that correspond to the physical stress. It can be translated with the metric: $\sigma^r_r = \sigma_{rr} = \sigma^{rr}$, $\sigma_{\theta\theta} = r^2 \sigma^\theta_\theta$, $\sigma^{\theta\theta} = \sigma^\theta_\theta / r^2$.

1.1.7   Energy density

The mechanics of plates may be described by local force balance equations: this is the Föppl-von Kármán equations; it may also be described by a local energy density containing stretching and bending terms:

$$\mathcal{E} = \frac{Y}{2(1 - v^2)} \left[(1 - v)\epsilon_{ij}\epsilon^{ij} + v\epsilon^i_i \epsilon^j_j \right] + \frac{B}{2} \left[(1 - v)c_{ij}c^{ij} + vc^i_i c^j_j \right]. \tag{1.47}$$

The stretching energy can be obtained by using the energy density $\mathcal{E}_\text{s} = \frac{Y}{2}\sigma_{ij}\epsilon^{ij}$ and the expression (1.16) for the stress. The bending energy $\mathcal{E}_\text{b}$ can be obtained in the same way by generalizing the calculation leading to Eq. (1.20).

As expected, the Föppl-von Kármán equations can be recovered from the energy density (1.47), although the derivation is not straightforward (see Audoly and Pomeau [2010], Chap. 6.6.3).

The strain used in the energy density (1.47) is defined by the difference between the metric and the rest metric which can correspond to a non-flat surface. Similarly, the rest surface can have a nonzero curvature; in this case, the difference between the actual curvature and the rest curvature should be used in the energy density.

The energy density (1.47) has thus two contributions, with coefficients given by the stretching and bending moduli Y and B, which scale differently with the thickness t of the plate: $Y \sim t$, $B \sim t^3$. In plate theory, one is often interested in the thin limit, $t \to 0$. From the scaling of the coefficients, it seems that the stretching energy needs to be minimized first, which amounts to look for isometric deformations. Then, the bending energy enters into play to select the isometric deformation with minimal energy. One should realize that the first step, identifying isometries, is far from obvious; we learn more about it in the next section about geometry.

1.2   Geometry

1.2.1   Gauss theorema egregium

We consider a shell with rest configuration

$$\bar{\boldsymbol{R}}(x, y) = \begin{pmatrix} x \\ y \\ \bar{\zeta}(x, y). \end{pmatrix} \tag{1.48}$$

We work in the *shallow shell* approximation, meaning that the shell is close to a planar surface. We ask the following question: is there a way to deform the shell in a surface with height $\zeta(x, y) = \bar{\zeta}(x, y) + w(x, y)$ without strain? In other words: can the in-plane displacement be chosen to cancel the strain? To answer this question, we wish to eliminate the in-plane displacement to obtain a relation between the strain and the out-of-plane displacement.

The rest metric of the shell is

$$\bar{g} = \begin{pmatrix} 1 + \bar{\zeta}_x^2 & \bar{\zeta}_x \bar{\zeta}_y \\ \bar{\zeta}_x \bar{\zeta}_y & 1 + \bar{\zeta}_y^2. \end{pmatrix} \tag{1.49}$$

The deformed shape reads

$$\boldsymbol{R}(x, y) = \begin{pmatrix} x + u(x, y) \\ y + v(x, y) \\ \zeta(x, y) \end{pmatrix}, \tag{1.50}$$

and the associated metric is

$$g = \begin{pmatrix} (1 + u_x)^2 + (\bar{\zeta}_x + w_x)^2 & (1 + u_x)u_y + v_x(1 + v_y) + (\bar{\zeta}_x + w_x)(\bar{\zeta}_y + w_y) \\ (1 + u_x)u_y + v_x(1 + v_y) + (\bar{\zeta}_x + w_x)(\bar{\zeta}_y + w_y) & (1 + v_y)^2 + (\bar{\zeta}_y + w_y)^2 \end{pmatrix}. \tag{1.51}$$

The strain is given by

$$\epsilon = \frac{g - \bar{g}}{2} = \begin{pmatrix} u_x + \frac{\zeta_x^2 - \bar{\zeta}_x^2}{2} & \frac{1}{2}[u_y + v_x + \zeta_x \zeta_y - \bar{\zeta}_x \bar{\zeta}_y] \\ \frac{1}{2}[u_y + v_x + \zeta_x \zeta_y - \bar{\zeta}_x \bar{\zeta}_y] & v_y + \frac{\zeta_y^2 - \bar{\zeta}_y^2}{2} \end{pmatrix} + O(u^2, v^2). \tag{1.52}$$

To get rid of the in-plane displacement, we consider the following combination:

$$\boxed{2\partial_x\partial_y\epsilon_{xy} - \partial_y^2\epsilon_{xx} - \partial_x^2\epsilon_{yy} = K - \bar{K},} \tag{1.53}$$

where

$$K = \det(\zeta_{ij}) = \zeta_{xx}\zeta_{yy} - \zeta_{xy}^2 \tag{1.54}$$

is the Gauss curvature of the deformed surface; $\bar{K}$ is the Gauss curvature of the rest configuration. Equation (1.53) is Gauss' "theorema egregium" (remarkable theorem).

The tensor ζ_{ij} being symmetric, there is an orthonormal base where it is diagonal; choosing this base, ζ reads

$$\zeta(x, y) = \frac{x^2}{2R_x} + \frac{y^2}{2R_y}, \tag{1.55}$$

where R_x and R_y are the two principal radii of curvature ($\kappa_i = 1/R_i$ is the corresponding curvature). Then

$$\zeta_{ij} = \begin{pmatrix} R_x^{-1} & 0 \\ 0 & R_y^{-1} \end{pmatrix} \tag{1.56}$$

and

$$K = \det(\zeta_{ij}) = \frac{1}{R_x R_y}. \tag{1.57}$$

Gauss theorem states that one cannot change the Gauss curvature of a shell without straining it, or that there is no isometry between surfaces with different Gauss curvature. Applied to an initially flat surface, it means that if the Gauss curvature of the deformed surface is non-zero (the sheet is bent in two directions), the strain cannot vanish. Since bending is energetically cheap and stretching is expansive, this is some kind of geometric frustration: bending in direction x is cheap, bending in direction y is also cheap, but bending in the two directions is expensive. This theorem also states that it is impossible to draw a planar map of the earth without deformation.

Application to the sheet-on-sphere adhesion.   By dimensional arguments, the "geometrical strain" required to apply a Gauss curvature K to a sheet of lateral size L is thus

$$\epsilon_{\text{Gauss}} \sim K L^2. \tag{1.58}$$

The stretching energy of a flat disc of radius L on a sphere of radius $R \gg L$ [Majidi and Fearing, 2008], where $K = R^{-2}$ is

$$U_{\text{stretch}} \sim Y L^2 \epsilon_{\text{Gauss}}^2 \sim Y K^2 L^6 \sim \frac{Y L^6}{R^4}. \tag{1.59}$$

The bending energy in this situation is

$$U_{\text{bend}} \sim \frac{B L^2}{R^2} \sim \frac{Y t^2 L^2}{R^2}. \tag{1.60}$$

With an adhesion energy Γ per unit area, if the sheet is sufficiently thin ($R > \ell_{\text{BC}} = \sqrt{B/\Gamma}$), the stretching energy sets the threshold for delamination, which is thus $\Gamma L^2 \sim U_{\text{stretch}}$ [Hure et al., 2011]. The sheet delaminates if

$$\frac{L}{R} > \left(\frac{\Gamma}{Y} \right)^{1/4}. \tag{1.61}$$

We will see later that this is actually a crude upper bound (Sec. 2.3.2).

1.2.2   Geometric rigidity of shells

We have seen in Sec. 1.2.1 that one cannot change the Gauss curvature of a plate or shell without straining it. We ask here a slighly different question: given a rest shape, can it be deformed isometrically, that is, without stretching? We focus here on infinitesimal displacements; when isometric, such displacements are called *infinitesimal bendings*.

The only condition that we obtained is Gauss' theorem (Eq. (1.53)), which we expand for small displacements $w(x, y) = \zeta(x, y) - \bar{\zeta}(x, y)$:

$$K - \bar{K} = \bar{\zeta}_{xx} w_{yy} + \bar{\zeta}_{yy} w_{xx} - 2 \bar{\zeta}_{xy} w_{xy} + O(w^2). \tag{1.62}$$

This quantity should be zero for the strain to vanish and the deformation to be a bending, leading to a partial differential equation (PDE) for the out-of-plane displacement $w(x, y)$. The type of equation is given by the determinant of the coefficients,

$$\det \begin{pmatrix} -\bar{\zeta}_{yy} & \bar{\zeta}_{xy} \\ \bar{\zeta}_{xy} & -\bar{\zeta}_{xx} \end{pmatrix} = \bar{\zeta}_{xx} \bar{\zeta}_{yy} - \bar{\zeta}_{xy}^2 = \bar{K}, \tag{1.63}$$

where $\bar{K}$ is the Gauss curvature of the rest configuration. The PDE for $w(x, y)$ is thus elliptic if the surface has a positive Gauss curvature, parabolic if its Gauss curvature is zero, and hyperbolic if its Gauss curvature is negative. The PDE can be of mixed type if the Gauss curvature of the surface changes sign, as for example in a torus.

A result of the theory of PDE is that the solution of an elliptic PDE is unique on a bounded surface if the boundary conditions are prescribed, or if the surface is closed, as a sphere, for instance. As a consequence, shells with positive Gauss curvature are more *rigid* than plates or shells with negative Gauss curvature.

This rigidity may explain why a spherical cap with vanishing bending modulus can impose its shape to a liquid interface [Timounay et al., 2021], contrary to a flat sheet [King et al., 2012, Schrecengost et al., 2025].

1.2.3 Developable surfaces

Here, we look for surfaces that are isometric to a plane; from Gauss' theorem, this means that they have a vanishing Gauss curvature, $K = 0$. Here we show how to integrate this local constraint into a global constraint and we use this global constraint to list all the ruled surfaces.

For simplicity we consider a surface that is close to a plane:

$$\boldsymbol{R}(x, y) = \begin{pmatrix} x \\ y \\ \zeta(x, y) \end{pmatrix}. \tag{1.64}$$

The curvature matrix $c_{ij} = \partial_i \partial_j \zeta$ is symmetric with zero determinant and trace $2H = c_{ii}$. We can thus write it as

$$c(x, y) = 2H(x, y) \begin{pmatrix} \sin(\phi(x, y))^2 & -\sin(\phi(x, y))\cos(\phi(x, y)) \\ -\sin(\phi(x, y))\cos(\phi(x, y)) & \cos(\phi(x, y))^2 \end{pmatrix}. \tag{1.65}$$

The functions $H(x, y)$ and $\phi(x, y)$ should satisfy the compatibility conditions

$$0 = \partial_y c_{xx} - \partial_x c_{xy} \tag{1.66}$$

$$= \partial_y \left[H \sin(\phi)^2 \right] + \partial_x \left[H \sin(\phi)\cos(\phi) \right] \tag{1.67}$$

$$= \partial_x H \sin(\phi)\cos(\phi) + \partial_y H \sin(\phi)^2 + H \left(\partial_x \phi \left[\cos(\phi)^2 - \sin(\phi)^2 \right] + 2\partial_y \phi \sin(\phi)\cos(\phi) \right) \tag{1.68}$$

and

$$0 = \partial_x c_{yy} - \partial_y c_{xy} \tag{1.69}$$

$$= \partial_x \left[H \cos(\phi)^2 \right] + \partial_y \left[H \sin(\phi)\cos(\phi) \right] \tag{1.70}$$

$$= \partial_x H \cos(\phi)^2 + \partial_y H \cos(\phi)\sin(\phi) + H \left(-2\partial_x \phi \cos(\phi)\sin(\phi) + \partial_y \phi \left[\cos(\phi)^2 - \sin(\phi^2) \right] \right). \tag{1.71}$$

Multiplying the first condition by $\cos(\phi)$, the second by $\sin(\phi)$, taking their difference and dividing by H, which we assume to be nonzero, we obtain

$$\cos(\phi)\partial_x \phi + \sin(\phi)\partial_y \phi = 0. \tag{1.72}$$

This equation can be solved by the method of characteristics: ϕ is constant along curves $(\hat{x}(s), \hat{y}(s))$ with $\hat{x}'(s) = \cos(\phi(\hat{x}(s), \hat{y}(s)))$ and $\hat{y}'(s) = \sin(\phi(\hat{x}(s), \hat{y}(s)))$; as a consequence, these curves are straight lines with slope ϕ. Along these lines, the height $\hat{\zeta}(s) = \zeta(\cos(\phi)s, \sin(\phi)s)$, satisfies

$$\hat{\zeta}''(s) = \cos(\phi)^2 c_{xx} + 2\cos(\phi)\sin(\phi)c_{xy} + \sin(\phi)^2 c_{yy} = 0. \tag{1.73}$$

This means that these lines are straight lines on the surface. Surfaces spanned by these lines are *ruled surfaces*.

We have shown that surfaces with vanishing Gauss curvature are ruled. To see whether the reverse is true, we compute the Gauss curvature of a ruled surface, which we parametrize as

$$\boldsymbol{R}(u, v) = \boldsymbol{a}(u) + v\boldsymbol{t}(u). \tag{1.74}$$

The vector $\boldsymbol{a}(u)$ describes the baseline and the vector $\boldsymbol{t}(u)$ gives the direction of the *generatrix*. Without loss of generality, we can impose $|\boldsymbol{a}'| = 1$, $|\boldsymbol{t}| = 1$, $\boldsymbol{a}' \cdot \boldsymbol{t} = 0$, where primes denote derivatives with respect to u. The metric of this surface is diagonal:

$$g = \begin{pmatrix} (\boldsymbol{a}' + v\boldsymbol{t}')^2 & 0 \\ 0 & 1 \end{pmatrix}. \tag{1.75}$$

The general expression of the Gauss curvature is given in Eq. (1.34); using the fact that the metric is diagonal, it is

$$K = c_u^u c_v^v - c_u^v c_v^u = g^{uu} g^{vv} \left(c_{uu} c_{vv} - c_{uv}^2 \right),$$
(1.76)

where $c_{ij} = \hat{\boldsymbol{n}} \cdot \partial_i \partial_j \boldsymbol{R}$. Since we are interested in the condition $K = 0$, we can discard the factor coming from the metric and we do not need to normalize the normal vector $\boldsymbol{n}$, which we can take equal to

$$\boldsymbol{n} = \partial_u \boldsymbol{R} \times \partial_v \boldsymbol{R} = (\boldsymbol{a}' + v\boldsymbol{t}') \times \boldsymbol{t}.$$
(1.77)

Since $\partial_v^2 \boldsymbol{R} = 0$, the Gauss curvature is c_{uv}^2; for it to be zero, we should have

$$0 = c_{uv} = \boldsymbol{n} \cdot \partial_u \partial_v \boldsymbol{R} = [(\boldsymbol{a}' + v\boldsymbol{t}') \times \boldsymbol{t}] \cdot \boldsymbol{t}' = (\boldsymbol{a}' \times \boldsymbol{t}) \cdot \boldsymbol{t}'.$$
(1.78)

From this characterization, we list all the developable surfaces. First, if $\boldsymbol{t}' = 0$, the surface is a *cylinder*. If $\boldsymbol{t}' \neq 0$, then we can write $\boldsymbol{a}'(u) = \lambda(u)\boldsymbol{t}(u) + \mu(u)\boldsymbol{t}'(u)$. We can define the new baseline $\tilde{\boldsymbol{a}} = \boldsymbol{a} - \mu\boldsymbol{t}$, which satisfies $\tilde{\boldsymbol{a}}' = (\lambda - \mu')\boldsymbol{t}$. If $\lambda = \mu'$, then $\tilde{\boldsymbol{a}}' = 0$, the surface is a *cone*. If $\lambda \neq \mu'$, the generatrix is along the tangent to the baseline, which defines a *tangent developable* surface.

1.2.4   3d shape design by prescribing the metric

Gauss' theorem gives a relation between the strain and the out-of-plane deformation. The strain being given as the difference between the actual and the target metric, this is actually a relation between the out-of-plane displacement and the metric. Prescribing a non-flat metric g^0, out-of-plane displacement may be needed for the strain to vanish.

Prescribing a non-flat metric can be done by using gels that have a non-uniform response to a solvent [Klein et al., 2007, Sharon and Efrati, 2010] or a temperature change [Kim et al., 2012], or "inflatable" elastomers [Siéfert et al., 2019] or patterned fabric [Siéfert et al., 2020]. This is not straightforward: in these cases, the metric that can be prescribed is either an isotropic dilatation, as for inflatable gels or a uniaxial dilatation or contraction, as for inflatable materials. The inverse problem is nevertheless numerically solvable Aharoni et al. [2018], Griniasty et al. [2019].

Note that the mapping between the metric and the out-of-plane displacement is not straightforward: a torn plastic sheet has a metric of the form [Marder et al., 2003]

$$\bar{g} = \begin{pmatrix} 1 + \alpha \mathrm{e}^{-y/\xi} & 0 \\ 0 & 1 \end{pmatrix},$$
(1.79)

where $x \in \mathbb{R}$ and $y \geq 0$. The line $y = 0$ being compressed in the flat state ($\epsilon_{xx} = \frac{1}{2}(g_{xx} - \bar{g}_{xx}) = -\alpha/2$), it buckles. Surprisingly, the buckling pattern is fractal [Sharon et al., 2002].

Finally, incompatibility between the target metric and the "spontaneous curvature" of the material can lead to specific buckling patterns, which occur for instance in plants [Armon et al., 2011].

1.3   Elasto-capillary phenomena

When solids are in contact with liquid interfaces, the surface tension γ of the interface can deform the solid. The lengthscale emerging from comparing the surface tension with the elasticity of the solid, set by its Young's modulus E, is the elasto-capillary length

$$\ell_{\mathrm{EC}} = \frac{\gamma}{E}.$$
(1.80)

Material	t (m)	E (Pa)	Y (N/m)	B (J)	ℓ_{BC} (m)
PDMS	6×10^{-5}	2×10^{6}	120	4×10^{-8}	7×10^{-4}
Polystyrene	1×10^{-7}	3×10^{9}	300	3×10^{-13}	2×10^{-6}

Table 1.1: Typical values of the thickness t, Young's modulus E, stretching modulus Y, bending modulus B and bendo-capillary length ℓ_{BC} for PDMS [Py et al., 2007] and polystyrene [Huang et al., 2007] sheets.

For an air-water interface $\gamma \simeq 72\,\mathrm{mN\,m^{-1}}$, and for a very soft gel $E \sim 1\,\mathrm{kPa}$, so that $\ell_{EC} \sim 0.1\,\mathrm{mm}$. The effect of surface tension can thus be observed easily [Style et al., 2013]. For stiffer solids the elasto-capillary length is in the nanometer range.

Liquid interfaces can instead easily deform slender bodies such as sheets. Orders of magnitude for two typical sheets are provided in Table 1.1. In both cases, surface tension is too small to stretch the sheet: $\gamma \ll Y$. To determine whether surface tension can bend the sheet, we define the bendo-capillary length

$$\ell_{BC} = \sqrt{B/\gamma}; \tag{1.81}$$

its typical magnitude is given in the last column of Table 1.1. This length is the typical radius of curvature that surface tension can generate; this also means that sheets longer than ℓ_{BC} can be bent, while sheets smaller than ℓ_{BC} cannot.

When the bendo-capillary length is smaller but not too far from the size of the sheet, as for PDMS sheets, surface tension can thus be used to create three dimensional structures from flat sheets: this is the so-called "capillary origami" [Py et al., 2007]. When this length is much smaller than the size of the sheet, surface tension can give rise to small scale features such as wrinkles [Huang et al., 2007, King et al., 2012] or folds [Paulsen et al., 2015].

Generally, surface tension is a convenient way to apply controlled loads to sheets to investigate their mechanical properties [Roman and Bico, 2010, Huang et al., 2007].

Chapter 2

Wrinkling, folding

Wrinkles are a special kind of buckling pattern forming in a variety of situations such as a poked inflated balloon [Vella et al., 2011], a hand streched band [Cerda and Mahadevan, 2003], or a drop supporting sheet on a liquid interface [Huang et al., 2007]. The main questions regarding wrinkles are: When do they form? What are their wavelength and amplitude?

First, we describe the wrinkles in a one-dimensional setting, focusing on the wrinkling threshold and the wavelength. Then, we discuss how this analysis is modified in two-dimensional configurations. Last, we consider the problem of finding the global shape of wrinkled structures.

2.1 Buckling on a foundation: wrinkling, folding

2.1.1 Wrinkling

As rods, plates easily buckle under a compression, and Euler buckling could also be encountered in plates. However, in many situations where plates buckle, there is a restoring force that pulls the plate back to the flat state. This force increases the buckling threshold and the buckling pattern, and usually leads to wrinkles.

2.1.1.1 Energetic approach

For simplicity, we here the buckling of a compressed plate lying on top of a liquid, typically at a water-air interface. Upon buckling, fluid has to be displaced, which costs gravitational energy. As a consequence, the "wavelength" is not set by the length of the plate, as with Euler buckling, but by a competition of bending and gravity, leading to a wrinkle pattern, which we characterize here.

A simple wrinkle pattern (with parallel and regular wrinkles) is characterized by the amplitude A of the wrinkles and their wavelength λ. The typical curvature is $R^{-1} \sim A/\lambda^2$, so that the bending energy per unit area is

$$U_{\text{bend}} \sim \frac{BA^2}{\lambda^4}, \tag{2.1}$$

On the other hand, it takes gravitational energy to displace liquid:

$$U_{\text{grav}} \sim \rho g A^2, \tag{2.2}$$

where ρ is the density difference between the two phases (below and above the sheet) and g is the grav-

itational acceleration. The compression is

$$\epsilon \sim \frac{A^2}{\lambda^2}. \tag{2.3}$$

First, we assume that the compression is imposed: Eq. (2.3) is a slaving condition between the amplitude and the wavelength. Cancelling the amplitude in the energies, we get $U_{\text{bend}} \sim B\epsilon/\lambda^2$, and $U_{\text{grav}} \sim \rho g \epsilon \lambda^2$. The total energy is minimal when these two energies are comparable, leading to

$$\boxed{\lambda \sim \left(\frac{B}{\rho g}\right)^{1/4}.} \tag{2.4}$$

Note that the wavelength does not depend on the compression. This length may be refered to as the bendo-gravity length. The corresponding energy is

$$\boxed{U_{\text{bendo}-\text{grav}} \sim \epsilon \sqrt{B\rho g}.} \tag{2.5}$$

This analysis is very common to determine how the wavelength depends on the parameters of the problem. Small wavelengths are usually penalized by the bending energy. On the contrary, many mechanisms can penalize large amplitudes, and thus large wavelengths via the slaving condition (2.3); they lead to the energy $U \sim KA^2$, where K is the "effective substrate stiffness". The origin can be gravity, elasticity of the substrate [Brau et al., 2011], or two-dimensional effects discussed in Sec. 2.2.1: tension or curvature in the transverse direction [Cerda and Mahadevan, 2003, Paulsen et al., 2016]. The resulting wavelength is thus

$$\lambda \sim \left(\frac{B}{K}\right)^{1/4}. \tag{2.6}$$

If we assume a compressive stress σ (we take $\sigma > 0$ for a compressive stress here), with an additional energy

$$U_{\text{comp}} \sim -\sigma\epsilon. \tag{2.7}$$

Wrinkles are favored when

$$\sigma > \sigma_{\text{c}} \sim \sqrt{B\rho g}. \tag{2.8}$$

This is just Euler buckling with a characteristic length set by λ instead of L.

2.1.1.2 Stability analysis

We can go beyond scaling analysis to get the buckling threshold. If the height of the film is given by $h(x)$, to lowest order in h the energy is given by

$$U = \frac{1}{2}\int \left[Bh''(x)^2 + \rho g h(x)^2 - \sigma h'(x)^2\right]\,\mathrm{d}x. \tag{2.9}$$

The corresponding Euler-Lagrange equation is

$$Bh^{(4)}(x) + \sigma h''(x) + \rho g h(x) = 0. \tag{2.10}$$

We look for a harmonic solution, $h(x) = A\cos(kx)$. The equation for k is

$$Bk^4 - \sigma k^2 + \rho g = 0. \tag{2.11}$$

It has a solution if $\sigma^2 - 4B\rho g > 0$, hence

$$\sigma_{\text{c}} = 2\sqrt{B\rho g}. \tag{2.12}$$

The solution is

$$k^* = \left(\frac{\rho g}{B}\right)^{1/4}, \tag{2.13}$$

corresponding to the wavelength found above.

2.1.2   Non-linearities, folding

In experiments of elastic sheets or even granular layers [Vella et al., 2004] sitting on top of a liquid, soon after wrinkles form they give way to a more localized deformation: a fold [Pocivavsek et al., 2008].

This phenomenon can be understood first from a simple scaling analysis. The total energy of the wrinkled state obtained upon compression of a sheet of length L by a length $\Delta = \epsilon L$ is (Eq. (2.5)):

$$U_{\mathrm{wr}} \sim \Delta \sqrt{B \rho g}. \tag{2.14}$$

On the other hand, an antisymmetric fold with two loops of size ℓ can take any amount of excess length with an energy $\ell[B\ell^{-2} + \rho g \ell^2]$ [Démery et al., 2014], leading to

$$U_{\mathrm{fold}} \sim \lambda \sqrt{B \rho g} \tag{2.15}$$

after optimizing over ℓ, where λ is the bendo-gravity length, Eq. (2.4). Forming a fold is thus energetically favorable for $\Delta > \lambda$, which occurs very quickly in long sheets.

To go beyond the scaling analysis, we can write the exact form of the energy associated to this problem. Denoting s the arclength along the sheet and $\phi(s)$ the angle between the sheet and an horizontal plane, the energy is

$$U = \frac{1}{2} \int \left[B\phi'(s)^2 + \rho g h(s)^2 \cos(\phi(s)) \right] \mathrm{d}s. \tag{2.16}$$

To be able to solve this problem using variational calculus, we should incorporate the relation between $h(s)$ and $\phi(s)$, $h'(s) = \sin(\phi(s))$, and the expression of the compressed length $\Delta = \int [1 - \cos(\phi(s))]\mathrm{d}s$. The functional to minimize is thus

$$I[h, \phi] = \int \left[\frac{B}{2}\phi'(s)^2 + \frac{\rho g}{2}h(s)^2 \cos(\phi(s)) - \sigma[1 - \cos(\phi(s))] - Q(s)[h'(s) - \sin(\phi(s))] \right] \mathrm{d}s. \tag{2.17}$$

Expanding to order h^2 and ϕ^2, we recover the linear equations of the previous section. The lowest non-linear order is obtained by expanding up to h^4; there the solution minimizing the energy is a modulated sinusoïd, representing localization with a characteristic length that is infinite at the buckling threshold and decreases after the threshold [Audoly, 2011]. This problem also admits an exact solution [Diamant and Witten, 2011]:

$$\phi(s) = 4 \arctan \left(\frac{\kappa \sin(ks)}{k \cosh(\kappa s)} \right), \tag{2.18}$$

where $k = \sqrt{2 + \sigma}/2$ and $\kappa = \sqrt{2 - \sigma}/2$ in dimensionless form (lengths rescaled by λ and energies by $\lambda \sqrt{B \rho g}$). Close to the transition $\kappa \ll 1$, this is a modulated sinusoid and the width of the modulation is κ^{-1}.

When the film rests on a gel instead of a liquid, the non-linearities of the substrate lead to period doubling [Brau et al., 2011]. Note that here the buckling of the film is obtained by bending the gel-film system.

2.2   Two-dimensional buckling

2.2.1   Selection of the wavelength

In the case of wrinkling at an air-water interface, the wavelength is set by a balance of bending and gravity (Sec. 2.1.1). Bending penalizes short wavelengths, while gravity penalizes large amplitudes, and

thus large wavelengths through the slaving condition. In two-dimensionnal settings, other mechanisms may penalize large amplitudes.

If wrinkles have a finite extent L and are submitted to a tension T, the stretching energy along the wrinkles is given by

$$U_{\text{tens}} \sim \epsilon T \sim \left(\frac{A}{L}\right)^2 T. \tag{2.19}$$

This corresponds to an effective stiffness [Cerda and Mahadevan, 2003]

$$K_{\text{tens}} = \frac{T}{L^2}. \tag{2.20}$$

This tension-induced stiffness has been shown to hold also for large amplitude wrinkles [He et al., 2023].

Wrinkles often occur on curved substrates. If the radius of curvature in the direction parallel to the wrinkles is $R_\parallel$, for a profile of the form $f(x) = A\cos(kx)$, the strain along the wrinkles at x is given by $\epsilon_\parallel(x) = f(x)/R_\parallel$. This leads to an average stretching energy

$$U_{\text{str}} \sim Y\left(\frac{A}{R_\parallel}\right)^2, \tag{2.21}$$

corresponding to an effective stiffness

$$K_{\text{curv}} = \frac{Y}{R_\parallel^2}. \tag{2.22}$$

This stiffness has been shown to affect the wavelength of wrinkles forming on an indented sheet [Paulsen et al., 2016].

2.2.2   Cascades

When describing the wrinkles that form on a compressed rectangular sheet in Sec. 2.1.1, we have assumed an infinite system in the direction of the wrinkles. However, the compressed sheet is always finite, and the capillary force at the edge of the sheet can modify the wrinkle pattern. As described by Huang et al. [2010], the capillary force favors shorter amplitude and wavelength, leading to a decrease of the wavelength close to the edge, which is a *cascade*.

A cascade is also observed on hanging curtains: the wavelength increases from the top to the bottom. Here we give the general analysis of Vandeparre et al. [2011], which uses the *wrinklon*, the transition zone between the wavelengths λ and 2λ, as the building block of a cascade. Considering that wrinkles with a wavelength λ have an amplitude A such that $\epsilon \sim A^2/\lambda^2$, the bending energy gain per unit area to double the wavelength is

$$U_{\text{bend}} \sim B\left(\frac{A}{\lambda^2}\right)^2 \sim \frac{B\epsilon}{\lambda^2}. \tag{2.23}$$

Here we have neglected the bending energy along the wrinkles. Changing the wavelength over a length L generates a strain $(A/L)^2$, and thus a stretching energy per unit area

$$U_{\text{str}} \sim Y\left(\frac{A}{L}\right)^4 \sim \frac{Y\epsilon^2\lambda^4}{L^4}. \tag{2.24}$$

Balancing these two energies leads to

$$L \sim \epsilon^{1/4}t^{-1/2}\lambda^{3/2}. \tag{2.25}$$

We note that we have set $U_{bend} \sim U_{str}$, while in principle we should have minimized $U_{bend} + U_{str}$, leading to $L \to \infty$; however, this is the energy per unit area, and minimizing $L\lambda(U_{bend} + U_{str})$ gives the result above.

Denoting x the coordinate along the wrinkles, we can obtain an equation for $\lambda(x)$:

$$\frac{d\lambda}{dx} \simeq \frac{\lambda}{L} \sim \epsilon^{-1/4} t^{1/2} \lambda^{-1/2}, \tag{2.26}$$

the solution of which is

$$\lambda \sim \epsilon^{-1/6} t^{1/3} x^{2/3}. \tag{2.27}$$

This scaling law has been observed for short curtains [Vandeparre et al., 2011].

If a tension σ is imposed along the wrinkles, this tension dominates over the strain induced by the period doubling if $\sigma \gg Y(A/L)^2$. If this is the case, the dominant stretching energy is

$$U_{str} \sim \sigma \left(\frac{A}{L} \right)^2 \sim \frac{\sigma \epsilon \lambda^2}{L^2} \tag{2.28}$$

instead of Eq. (2.24). Comparing this energy to the bending energy, we find

$$L \sim \left(\frac{\sigma \lambda^4}{B} \right)^{1/2} \sim \left(\frac{\sigma}{Y} \right)^{1/2} \frac{\lambda^2}{t}. \tag{2.29}$$

With the same argument as above, we have

$$\frac{d\lambda}{dx} \sim \left(\frac{\sigma}{Y} \right)^{-1/2} \frac{t}{\lambda}, \tag{2.30}$$

and thus

$$\lambda \sim \left(\frac{\sigma}{Y} \right)^{-1/4} t^{1/2} x^{1/2}. \tag{2.31}$$

This scaling has been observed for long curtains, graphene sheets under tension [Vandeparre et al., 2011], and at the edge of a compressed floating sheet [Huang et al., 2010].

Note that the energies (2.19) and (2.28) are exactly the same, meaning that no cascade can be observed for wrinkles whose wavelength is determined by the tension. This explain why the wavenumber is constant in a hanging water balloon [He et al., 2023].

Note that the cascade described here is very different from the cascade observed at the edge of a torn plastic sheet, where the different wavelength superpose [Sharon et al., 2002, Marder et al., 2003, Sharon et al., 2007].

2.2.3 Folds and crumples

When wrinkles are curved, the curvature generate a strain that can play a role in the wavelength selection, as seen in Sec. 2.2.1. However, when this curvature is too large the wrinkles are replaced by "crumples"; they can be seen when a flat circular sheet is placed of a drop with increasing curvature [King et al., 2012], or in an inflated Mylar balloon [Timounay et al., 2020]. The precise shape of the crumples, their energy, and the critical curvature where they appear are still unknown.

Sharp folds are another pattern that appear upon compression in two-dimensional settings; they have been observed in a "sheet on drop" experiment [Paulsen et al., 2015] or in the Lamé setup when $T_{in}R_{in} > T_{out}R_{out}$ (see Sec. 2.4.1) [Piñeirua et al., 2013, Paulsen et al., 2017].

Up to now, we do not know how to describe the mechanics of individual crumples and folds. As folds concentrate excess material, they allow the sheet to adopt shapes that cannot be achieved with wrinkles, and they may be favored for this reason, as discussed in Sec. 2.4.

We come back to the crumples in Sec. 3.4.

2.3   Rucks and blisters

A sheet compressed on an undeformable substrate has to depart from the substrate when it buckles. The energetic cost of leaving the substrate can either be a continuous function of the distance to the substrate, for instance if it is due to gravity, as for a ruck in a rug [Vella et al., 2009, Kolinski et al., 2009], or discontinuous, as for delamination from a liquid covered substrate [Bense et al., 2020, Box et al., 2023]. We discuss first delamination upon uniaxial compression and then the consequences for the sheet on sphere adhesion.

2.3.1   Delamination upon uniaxial compression

We resort to a scaling analysis to investigate the threshold for delamination and the properties of the final ruck or *blister*, following the analysis of Davidovitch and Démery [2021]. We compare the energy of the compressed sheet attached to the substrate, U_{comp}, and the energy of the blister, U_{bl}. For a sheet of length L compressed by an amount Δ, the compression is $\epsilon = \Delta/L$ and the energy is $U_{\mathrm{comp}} \sim LY\epsilon^2 \sim L\Delta^2/L$. Introducing the normalized energy $u = U/(YL)$, we obtain

$$u_{\mathrm{comp}} \sim \epsilon^2. \tag{2.32}$$

To describe a blister with width λ and amplitude A, we assume the sheet to be inextensible (Fig. 2.1(a)), which sets $\Delta \sim \lambda \times (A/\lambda)^2 \sim A^2/\lambda$, hence $A \sim \sqrt{\Delta\lambda}$. The energy of a blister contains the bending energy U_{bend}. In the small slope approximation, $A/\lambda \sim \sqrt{\Delta/\lambda} \ll 1$, the curvature can be estimated to A/λ^2, so that the bending energy is $U_{\mathrm{bend}} \sim B\lambda(A/\lambda^2)^2 \sim B\Delta/\lambda^2$:

$$u_{\mathrm{bend}} \sim \frac{B\Delta}{YL\lambda^2} \sim \frac{\tau\epsilon}{\ell^2}, \tag{2.33}$$

where we have defined the dimensionless quantities

$$\tau = \frac{t^2}{L^2} \sim \frac{B}{YL^2}, \tag{2.34}$$

$$\ell = \frac{\lambda}{L}. \tag{2.35}$$

The energy of a blister also contains the cost to depart from the substrate, $U_{\mathrm{d}} \sim \lambda f_{\mathrm{d}}(A)$, where $f_{\mathrm{d}}(A) = \rho g A$ for gravity and $f_{\mathrm{d}}(A) = \Gamma$ for adhesion with a surface energy Γ. We focus on adhesion in the following, but rucks can be treated in the same way. The dimensionless departure energy is thus

$$u_{\mathrm{d}} \sim \frac{\lambda\Gamma}{YL} \sim \gamma\ell, \tag{2.36}$$

where we have defined the last dimensionless quantity

$$\gamma = \frac{\Gamma}{Y}. \tag{2.37}$$

To determine the blister width, the bending energy should match the delamination energy, $u_{\mathrm{bend}} \sim u_{\mathrm{d}}$, leading to

$$\ell = \left(\frac{\tau\epsilon}{\gamma}\right)^{1/3}, \tag{2.38}$$

$$u_{\mathrm{bl}} = (\tau\epsilon)^{1/3}\gamma^{2/3}. \tag{2.39}$$

The energy increase with the compression ϵ gives the stress $\sigma = -\partial U/\partial L = -Y \partial u/\partial \epsilon$:

$$\sigma_{\text{bl}} \sim Y\tau^{1/3}\gamma^{2/3}\epsilon^{-2/3}. \tag{2.40}$$

The stress decreases as compression increases at odds with wrinkles, where the stress is constant, as can be seen from Eq. (2.5).

For the description of a blister above to be consistent, the slope should indeed be small, that is $1 \gg \Delta/\lambda \sim \epsilon/\ell$. With the width obtained above (Eq. (2.38)), this condition reads

$$\tau \gg \gamma\epsilon^2. \tag{2.41}$$

This means that the sheet should be thick enough, and that the compression should be small enough. As the compression increases, the slope will become large at some point, and the blister transitions to a fold; this is reminiscent of the wrinkle-fold transition described in Sec. 2.1.2 (Fig. 2.1(b)). For the fold, the amplitude is comparable to the width of the fold, so that the bending energy is $U_{\text{bend}} \sim B/\lambda$ or, in dimensionless form

$$u_{\text{bend}} \sim \frac{B}{YL\lambda} \sim \frac{\tau}{\ell}. \tag{2.42}$$

Comparing it to the delamination energy (2.36), we obtain the width and energy of a fold:

$$\ell \sim \sqrt{\tau/\gamma} \sim \ell_{\text{BC}}/L, \tag{2.43}$$
$$u_{\text{f}} \sim \sqrt{\gamma\tau}, \tag{2.44}$$

where ℓ_{BC} is the bendo-capillary length (1.81). Since the fold energy does not depend on the compression, the stress is zero.

The threshold for delamination can then be obtained by comparing the energy of the compressed laminated state (Eq. (2.32)) to the energy of the buckled configuration (Eq. (2.39) or (2.44)). When the condition (2.41) is satisfied, the buckled configuration is a blister and the delamination threshold is $\epsilon^* \sim (\gamma^2\tau)^{1/5}$. At this compression, the condition (2.41) reads $\tau \gg \gamma^3$. When the buckled configuration is a fold, the delamination threshold is $\epsilon^* \sim (\gamma\tau)^{1/4}$. Finally, we obtain the phase diagram shown in Fig. 2.1(c).

2.3.2 Application to the sheet-on-sphere adhesion

We come back to the problem of a circular sheet with radius L placed on a sphere with radius R with an adhesion energy Γ per unit area (Sec. 1.2.1). By comparing the energy of the fully adhered state coming from the stretching energy due to the Gauss curvature mismatch to the energy of the flat delaminated state, we found (Eq. (1.61)) that delamination occurs for

$$\Lambda > \beta^{1/4}, \tag{2.45}$$

where we have defined

$$\Lambda = L/R. \tag{2.46}$$

However, the estimate of the energy of the delaminated state is a crude upper bound: it is much more favorable to delaminate along radial blisters, as can be seen in experiments [Hure et al., 2011, Box et al., 2023], instead of leaving the sphere as a whole.

In order to estimate the energy of the state with radial blisters, one as to balance the energy of the blisters, which increases with the number of blisters, with the "Gauss energy" of the area between the blisters, which decreases with the number of blisters [Box et al., 2023]. Taking into account the fact that
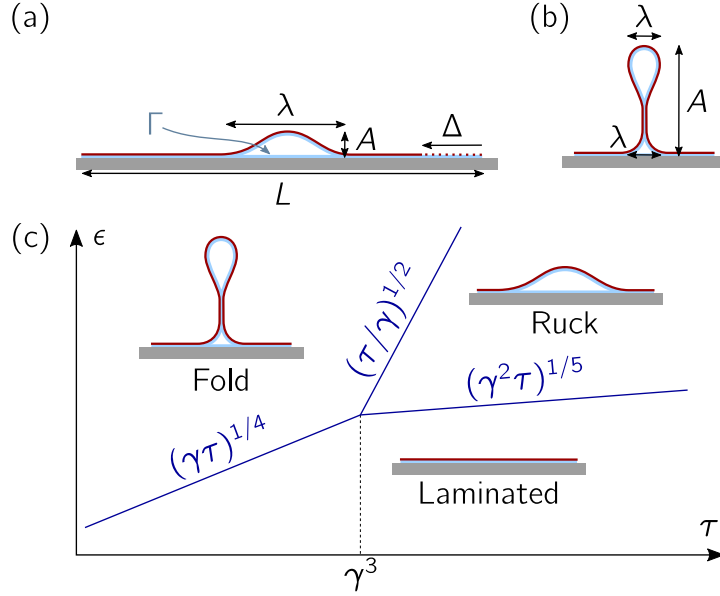
Figure 2.1: Delamination upon compression. (a) Small slope blister. (b) Large slope fold. (c) Phase diagram. Adapted from Davidovitch and Démery [2021].

delamination can occur through blisters or folds, the analysis of Box et al. [2023] gave the following delamination thresholds:

$$\Lambda^* \sim \begin{cases} \gamma^{1/2} & \text{if } \tau \ll \gamma^4 \\ (\tau\gamma^2)^{1/12} & \text{if } \gamma^4 \ll \tau \ll \gamma \end{cases} \tag{2.47}$$

where we have redefined

$$\tau = \frac{B}{YR^2}. \tag{2.48}$$

The first case corresponds to the situation where the sheet bends easily, and it delaminate into folds as soon as its edge is under compression, which is why the threshold does not depend on τ. This threshold is much smaller than the one obtained previously ($\gamma^{1/2} \ll \gamma^{1/4}$). The second case corresponds to the situation where the sheet delaminates into rucks that require a finite compression, thereby delaying delamination. When $\tau > \gamma$, the adhesion is not sufficient to bend the sheet, which delaminates as a whole; when $\tau \sim \gamma$, the estimate of Hure et al. [2011] is recovered.

2.4 Post-buckling behavior and reduced models

The Föppl-von Kármán equations are non-linear and may thus be difficult to solve. Moreover, when wrinkles or folds appear, it becomes hopeless to solve at the same time for the global shape of the plate and for the microstructure (wrinkles, folds, etc.). To address such situation, it is always useful to have reduced models. We will also see that such reduced model allows to determine the location of wrinkles far beyond the buckling threshold.

2.4.1 Membrane model

Neglecting the bending contribution in Eq. (1.30), we obtain the membrane model. However, we know from the study of buckling (Sec. 2.1) that without bending modulus there is no resistance to compression,
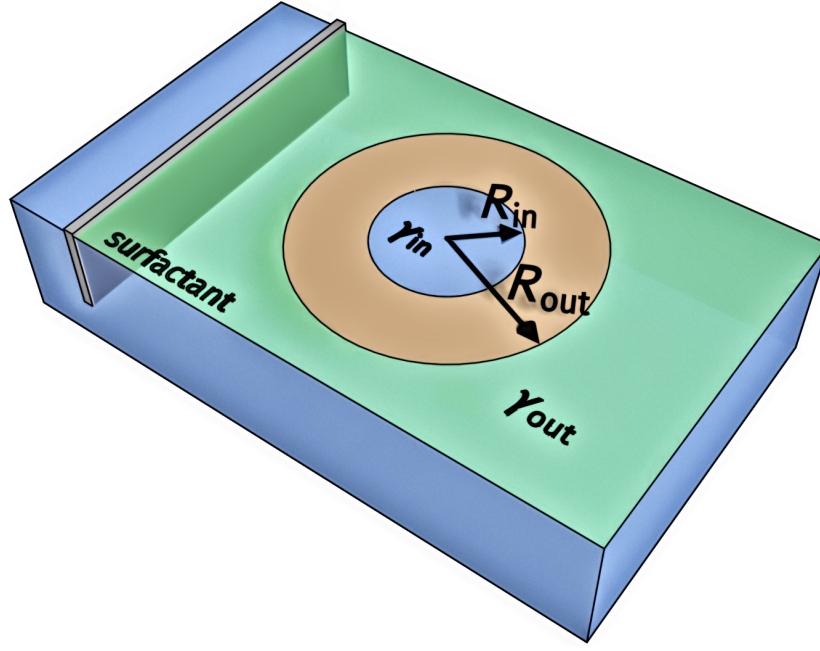
Figure 2.2: Lamé setup

meaning that any level of compression is relaxed by tiny wrinkles, which cannot be described by the membrane model. The absence of compressive stress should be added to the equations:

$$\sigma_{ii} \geq 0, \tag{2.49}$$

for any direction i. Moreover, when wrinkles form ($\sigma_{ii} = 0$), the Hooke's law (1.16) breaks down and the system compress freely, meaning that $\epsilon_{ii} \leq 0$. The resulting theory for the stress field is also called *tension field theory* [Mansfield, 1969, Davidovitch et al., 2011].

A refined version of the membrane model accounts for the fact that there is a small residual compressive stress in the wrinkled state, which is given by the wrinkling threshold (Eq. (2.8)):

$$\sigma_{ii} \geq -\sqrt{BK}, \tag{2.50}$$

where K is the effective substrate stiffness, $K = \rho g$ for a liquid interface under gravity. This stress plays a role in the configuration of a flat sheet attached to an elastic sphere [Davidovitch et al., 2019].

In elastocapillary problems, the bending modulus may be assumed to be negligible when the bendo-capillary length is much smaller than the other characteristic lengths of the problem. This is the case for polystyrene sheets, but not really for PDMS sheets (see Table 1.1).

The Lamé problem. The "Lamé setup" is shown Fig. 2.2. The idea is to apply different tensions on the inner and outer edges (T_{in} and T_{out}) of an annular sheet. To do so, the sheet is placed at a water-air interface and a surfactant is added outside of the annulus, the tension is thus lower on the outer edge ($T_{out} < T_{in}$). Moving a barrier allows to compress the surfactant layer and thus to lower the outer surface tension. This setup has been developed by Piñeirua et al. [2013] and used with thinner sheets by Paulsen et al. [2017]. Géminard et al. [2004] have used a setup with the same geometry but applying loads differently.

The main parameters are the inner and outer radii R_{in} and R_{out}, and the inner and outer surface tension T_{in} and T_{out}. In experiments, T_{out} is lowered. At some point, wrinkles form near the inner edge and expand.

Flat state. We start by computing the displacement and stress field in the flat state. Due to the axial symmetry of the problem, the displacement is radial and depends on the distance r to the center of the annulus, we denote it $u(r)$. The displacement is the function that we have to determine. The strain in the radial and azimuthal directions can easily be computed:

$$\epsilon_{rr}(r) = \partial_r u(r), \tag{2.51}$$

$$\epsilon_{\theta\theta}(r) = \frac{u(r)}{r}. \tag{2.52}$$

It is related to the stress through Hooke's law (1.16).

The force balance equation can be determined either by considering the forces on a small piece of sheet or by using covariant elasticity with the metric corresponding to the polar coordinates. Due to the symmetry of the problem, it provides an equation only in the direction r:

$$\partial_r [r\sigma_{rr}(r)] = \sigma_{\theta\theta}. \tag{2.53}$$

Finally, the boundary conditions are:

$$\sigma_{rr}(R_{\text{in}}) = T_{\text{in}}, \tag{2.54}$$

$$\sigma_{rr}(R_{\text{out}}) = T_{\text{out}}. \tag{2.55}$$

The Hooke's law gives

$$\sigma_{rr}(r) = \frac{Y}{1 - v^2} \left[u'(r) + v\frac{u(r)}{r} \right], \tag{2.56}$$

$$\sigma_{\theta\theta}(r) = \frac{Y}{1 - v^2} \left[\frac{u(r)}{r} + vu'(r) \right]. \tag{2.57}$$

The radial force balance (2.53) thus becomes

$$\partial_r [ru'(r)] = \frac{u(r)}{r}. \tag{2.58}$$

Looking for a solution of the form $u(r) = r^\alpha$, we get $\alpha^2 = 1$, hence

$$u(r) = Ar + \frac{B}{r}. \tag{2.59}$$

Hence

$$\sigma_{rr}(r) = \frac{Y}{1 - v^2} \left[(1 + v)A - (1 - v)\frac{B}{r} \right] = A' + \frac{B'}{r^2}. \tag{2.60}$$

Using the boundary conditions (2.54, 2.55), we obtain

$$\sigma_{rr}(r) = \frac{R_{\text{out}}^2 T_{\text{out}} - R_{\text{in}}^2 T_{\text{in}}}{R_{\text{out}}^2 - R_{\text{in}}^2} + \frac{T_{\text{in}} - T_{\text{out}}}{R_{\text{in}}^{-2} - R_{\text{out}}^{-2}} \frac{1}{r^2}, \tag{2.61}$$

$$\sigma_{\theta\theta}(r) = \frac{R_{\text{out}}^2 T_{\text{out}} - R_{\text{in}}^2 T_{\text{in}}}{R_{\text{out}}^2 - R_{\text{in}}^2} - \frac{T_{\text{in}} - T_{\text{out}}}{R_{\text{in}}^{-2} - R_{\text{out}}^{-2}} \frac{1}{r^2}. \tag{2.62}$$

where we have used the force balance (2.53) to compute the azimuthal stress. Introducing

$$T_\infty = \frac{R_{\text{out}}^2 T_{\text{out}} - R_{\text{in}}^2 T_{\text{in}}}{R_{\text{out}}^2 - R_{\text{in}}^2} < T_{\text{in}}, \tag{2.63}$$

the stress field can be written as

$$\sigma_{rr}(r) = T_\infty + (T_{\text{in}} - T_\infty)\frac{R_{\text{in}}^2}{r^2}, \tag{2.64}$$

$$\sigma_{\theta\theta}(r) = T_\infty - (T_{\text{in}} - T_\infty)\frac{R_{\text{in}}^2}{r^2}. \tag{2.65}$$

As $\sigma_{\theta\theta}(R_{\text{in}}) = 2T_\infty - T_{\text{in}}$, the inner edge is under compression for $T_\infty < T_{\text{in}}/2$, and prone to buckling.

Near threshold. We first consider a narrow annulus, $R_{\text{out}} \gtrsim R_{\text{in}}$, so that the azimuthal stress is almost uniform. Its buckling can be seen as the buckling of a compressed sheet on a liquid, which has been discussed in Sec. 2.1.1. The threshold is thus $\sigma_{\theta\theta} < -2\sqrt{B\rho g}$, and the wavelength should be given by $\lambda = 2\pi(\rho g/B)^{1/4}$; the criterion for the stress can be written

$$\frac{T_\infty}{T_{\text{in}}} < \frac{1}{2} - \frac{\ell_{\text{BC}}}{\ell_{\text{c}}}, \tag{2.66}$$

where $\ell_{\text{c}} = \sqrt{T_{\text{in}}/(\rho g)}$ is the capillary length. These predictions have been verified experimentally [Piñeirua et al., 2013]. We have neglected the effect of the meniscus of liquid on the inner and outer edges, in the one dimensional analysis of Sec. 2.1.1 the sheet was assumed to be infinite in the direction perpendicular to the compression. As explained by Piñeirua et al. [2013], this assumption is valid if the annulus is wider than the capillary length and stiff enough to prevent a cascade at its edges, an effect that we discuss below.

The arguments for a narrow annulus provide handwavy arguments for a wider annulus. The threshold for buckling can alternatively obtained by a linear stability analysis, using the out-of-plane Föppl-von Kármán equation (1.31) [Piñeirua et al., 2013]. Denoting $w(r, \theta)$ the vertical displacement of the sheet, the pressure is given by $P = -\rho g w$ and

$$B\nabla^4 w - \sigma_{rr}\left(\partial_r^2 w + \frac{1}{r}\partial_r w\right) - \sigma_{\theta\theta}\frac{1}{r^2}\partial_\theta^2 w + \rho g w = 0. \tag{2.67}$$

Looking for a solution of the form $w(r, \theta) = f(r)\sin(m\theta)$, the above equation becomes a fourth order ODE for $f(r)$. Assuming that the sheet is free of forces and torques at the inner and outer edges leads four boundary conditions. Generically, the only solution to this problem is $f(r) = 0$; the linear stability analysis amounts to look for the value of T_{out} where a non-zero solution exists. The value of m leading to the highest value of $T_{\text{out,c}}$ gives the wavelength of the wrinkles, and the form of $f(r)$ gives their extent.

Far from threshold. We assume that we are far above the buckling threshold and want to determine the properties of the wrinkles. In this situation the wrinkles substantially modify the stress field; we take the membrane limit and assume that the wrinkles completely relax the compression: $\sigma_{\theta\theta} = 0$ where wrinkles are present, and $\sigma_{\theta\theta} > 0$ without wrinkles (the same condition applies to σ_{rr}, but it is always positive) [Davidovitch et al., 2011].

The annulus is thus separated in two regions: a wrinkled region for $R_{\text{in}} < r < W$, where $\sigma_{\theta\theta} = 0$ and a flat region for $W < r < R_{\text{out}}$, where $\sigma_{\theta\theta} > 0$. In the wrinkled region, the force balance (2.53) gives $\sigma_{rr}(r) = T_{\text{in}}R_{\text{in}}/r$. In the flat region, the equations are the same as above, and the stress field is of the

form $\sigma_{rr}(r) = A + B/r^2$, $\sigma_{\theta\theta}(r) = A - B/r^2$. The boundary conditions are $\sigma_{rr}(W) = T_{\text{in}}R_{\text{in}}/W$, $\sigma_{\theta\theta}(W) = 0$, and $\sigma_{rr}(R_{\text{out}}) = T_{\text{out}}$. The first two equations give $B = AW^2$ and $A = T_{\text{in}}R_{\text{in}}/(2W)$, and the last equation leads to an equation for $x = W/R_{\text{out}}$:

$$x^2 - 2\alpha x + 1 = 0, \tag{2.68}$$

where

$$\alpha = \frac{T_{\text{out}}R_{\text{out}}}{T_{\text{in}}R_{\text{in}}}. \tag{2.69}$$

This equation has a real solution $x < 1$ only if $\alpha > 1$, which is

$$x^* = \alpha - \sqrt{\alpha^2 - 1}. \tag{2.70}$$

Note that there is no solution if $\alpha < 1$.

In the wrinkled region, the amplitude and wavelength of the wrinkles are related by a slaving condition anologous to the one seen in Sec. 2.1.1 (Eq. (2.3)). Assuming an out of plane displacement of the form $w(r, \theta) = f(r)\sin(m\theta)$, the relative excess length taken away by the wrinkles at a radius r is $m^2 f(r)^2/(4r^2)$ in the limit of small slopes. This strain should be added to the strain of the flat state (Eq. (2.52)):

$$\epsilon_{\theta\theta}(r) = \frac{u(r)}{r} + \frac{m^2 f(r)^2}{4r^2}. \tag{2.71}$$

Given the stress field, we can compute the strain through the Hooke's law, which gives $\epsilon_{rr} = \sigma_{rr}/E$ and $\epsilon_{\theta\theta} = -\nu\epsilon_{rr}$ in the wrinkled zone. The strain field can then be integrated to get $u(r)$, so that we finally have determined $mf(r)$ through Eq. (2.71).

2.4.2   Geometric model

An even further simplification if the loading is too weak to stretch the sheet is to consider the sheet as inextensible. This can be called a "geometric" model, in the sense that there is no elastic modulus anymore.

In elastocapillary problems, the loading is due to surface tension γ, so that the sheet can be considered as inextensible if $\gamma \ll Y$. Note that, although this condition is often satisfied (see Tab. 1.1), it may sometimes lead to a fully wrinkled sheet and diverging stresses; as a consequence, the geometric model cannot be used to predict the extent of the wrinkled zone for a sheet on drop [King et al., 2012], a spherical shell on a flat liquid interface [Timounay et al., 2021], or in the Lamé problem discussed above [Davidovitch et al., 2011].

Example: shape of a Mylar balloon.   This geometric model has been used to understand the shape of a Mylar balloon [Paulsen, 1994]; we quickly review its approach here. A Mylar balloon is made of two flat discs glued together at the edges, and then inflated. Assuming that Mylar is inextensible, once under pressure, the balloon takes the shape that maximizes its volume under the constraint of inextensibility.

Taking a cut of the balloon along its symmetry axis, a quarter of the shape can be described by a function $y(x) \geq 0$ for $0 \leq x \leq a$, where a is the radius of the inflated balloon, such that $y(a) = 0$. The volume V of the balloon and half length of a meridian R (the radius of the disks) are given by

$$V = 4\pi \int_0^a x\,y(x)\mathrm{d}x, \tag{2.72}$$

$$R = \int_0^a \sqrt{1 + y'(x)^2}\mathrm{d}x \tag{2.73}$$

The functionnal to minimize is thus

$$I[y] = \int_0^a \left[xy(x) - \lambda \sqrt{1 + y'(x)^2} \right] dx, \tag{2.74}$$

where λ is a Lagrange multiplier and we have factored out 4π.

The corresponding Euler-Lagrange equation reads

$$-\lambda \frac{d}{dx} \left[\frac{y'(x)}{\sqrt{1 + y'(x)^2}} \right] = x. \tag{2.75}$$

It can be shown rigorously that the boundary conditions are $y'(0) = 0$, $y'(a) = -\infty$. Integrating the above equation between 0 and x leads to

$$\frac{y'(x)}{\sqrt{1 + y'(x)^2}} = -\frac{x^2}{a^2}, \tag{2.76}$$

Where we have used $y'(a) = -\infty$ to show that $\lambda = a^2/2$. This relation can be inverted, leading to

$$y'(x) = -\frac{x^2}{\sqrt{a^4 - x^4}}. \tag{2.77}$$

This completely defines the solution through an elliptic integral:

$$y(x) = \int_x^a \frac{x'^2}{\sqrt{a^4 - x'^4}} dx'. \tag{2.78}$$

This approach is purely geometric and bypasses the complex pattern of the wrinkles and "crumples" that appear in these balloons. The calculation could also be done using mechanical arguments: this is the approach followed by Taylor to compute the optimal shape of a parachute [Taylor, 1919]. Quite surprisingly, the parachute has the same shape as the balloon.

Back to the Lamé problem. The solution to the Lamé problem in the membrane limit presented above does not exist for (Eq. (2.68))

$$\alpha = \frac{T_{\text{out}} R_{\text{out}}}{T_{\text{in}} R_{\text{in}}} < 1. \tag{2.79}$$

When α approaches 1 from above, the extent of the wrinkled zone approaches 1 from below, meaning that the sheet becomes fully wrinkled (Eq. (2.70)). For $\alpha < 1$, the outer tension is not strong enough to resist the inner tension and the sheet has to move inward, and the displacement is finite, which explains why the membrane approach fails. In order to describe the behavior of the sheet in the regime $\alpha < 1$, we use the geometric model, following Paulsen et al. [2017].

We first consider an axisymmetric deformation: the sheet moves inward by a uniform radial displacement $u \leq 0$, the inequality coming from the inextensibility of the sheet. We write the energy of the system, which in the geometric model originates only from surface energy; we may write it as

$$U_{\text{surf}} = \pi (R_{\text{in}} + u)^2 T_{\text{in}} - \pi (R_{\text{out}} + u)^2 T_{\text{out}}. \tag{2.80}$$

For the outer area, we have removed the area of the reservoir, which is constant and does not depend on u. Minimizing the energy with respect to $u \leq 0$ yields $u = 0$ for $\alpha > 1$ and, for $\alpha < 1$:

$$u = -\frac{T_{\text{in}} R_{\text{in}} - T_{\text{out}} R_{\text{out}}}{T_{\text{in}} - T_{\text{out}}}, \tag{2.81}$$

$$\Delta U_{\text{surf}} = -\pi \frac{(T_{\text{in}} R_{\text{in}} - T_{\text{out}} R_{\text{out}})^2}{T_{\text{in}} - T_{\text{out}}}. \tag{2.82}$$

We see that there is always a well defined solution because $u + R_{\text{in}} > 0$.

However, the experiments do not display such inward motion [Paulsen et al., 2017]. For wide annuli, instead, two parts of the sheet seem to move rigidly toward each other. The inner and outer areas can also be computed for this displacement field:

$$U_{\text{surf}} = 2 \left[T_{\text{in}} R_{\text{in}}^2 \phi \left(-\frac{u}{R_{\text{in}}} \right) - T_{\text{out}} R_{\text{out}}^2 \phi \left(-\frac{u}{R_{\text{out}}} \right) \right], \tag{2.83}$$

$$\phi(x) = \cos^{-1}(x) - x\sqrt{1 - x^2}. \tag{2.84}$$

Minimizing with respect to u yields

$$u = - \left(\frac{T_{\text{in}}^2 R_{\text{in}}^2 - T_{\text{out}}^2 R_{\text{out}}^2}{T_{\text{in}}^2 - T_{\text{out}}^2} \right)^{1/2}, \tag{2.85}$$

and an energy that can be computed numerically and that is smaller than for the axisymmetric solution [Paulsen et al., 2017]. The geometric model thus explains the appearance of folds from the fact that a global shape with folds is more efficient than a global shape with wrinkles; this explanation has nothing to do with the energy of the folds, which is assumed to be negligible here.

The 2-fold solution is not always the lowest energy one: for narrow annuli, a "collapsed racetrack" shape has a lower energy and seems to correspond to the experimental observations.

One should note that we have not "derived" these shapes through functional energy minimization or force balance; instead, we have guessed non axisymmetric shapes based on experimental observations, which turned out to have a lower energy than the best axisymmetric solution. This is enough to prove that the minimal energy solution is not axisymmetric.

Wrapping.   We have seen that the geometric model allows us to deal with situations with a much larger confinement than the force balance equations. This is also true for the sheet on drop experiment: while the membrane model has successfully predicted the extent of wrinkles [King et al., 2012], it is limited to a small slope axisymmetric configuration.

When the slope is large, that is, when the sheet begins to wrap the liquid, experiments show that the sheet breaks axisymmetry and adopts a polygonal shape when viewed from above Paulsen et al. [2015]. At complete wrapping, the best shape is the one that encloses the largest volume of liquid. The best axisymmetric shape is the balloon shape discussed above. It is not difficult to devise axisymmetry breaking shapes that enclose a larger volume of liquid, again showing that the system breaks axisymmetry at large deformations of the global shape.

As for the Lamé problem, some of the symmetry breaking shapes involve the localization of excess material, which could correspond to the experimentally observed folds.

2.4.3   Models for the wrinkle patterns

The membrane model aims at describing the stress field coarse-grained over the wrinkles and the wrinkled zones; the geometric model targets gross shapes with large deformations. In order to describe the wrinkle patterns, such that the orientation of the wrinkles, their amplitude, and their wavelength, one can build on the stress and strain fields of the membrane model, as described above. However, this approach has mostly been used in cases where the orientation of the wrinkles is known, for example where the system is axisymmetric and the wrinkles radial. The models described below aim at describing the wrinkles patterns in more complex situations.

Smectic model for wrinkles. The analysis of Aharoni et al. [2017] is based on observations of the wrinkle patterns of a spherical shell placed on a flat liquid interface, but aims at being general. The initial metric of the shell is $\bar{g}_{ij}$, and its final shape is described by the height field

$$\zeta(\boldsymbol{r}) = a(\boldsymbol{r}) \cos(\phi(\boldsymbol{r})), \tag{2.86}$$

where $\boldsymbol{r} = (x, y)$; $a(\boldsymbol{r})$ is the amplitude of the wrinkled pattern and $\phi(\boldsymbol{r})$ is the phase. The phase gradient is the wavevector, $\nabla\phi(\boldsymbol{r}) = \boldsymbol{k}(\boldsymbol{r})$, which gives the orientation and the wavelength of the wrinkles. The goal of Aharoni et al. [2017] was to write down a theory for the amplitude and the wavevector that coarse-grains the individual wrinkles. They arrived at the effective energy density

$$U = \frac{Y}{8} \left| \delta_{ij} + \frac{a^2}{2} k_i k_j - \bar{g}_{ij} \right|^2 + \frac{\sigma\epsilon}{4} \left(\lambda_0^2 k^2 - 1 \right)^2 + \frac{Y \lambda_0^4 \epsilon^2}{256} |\partial_i k_j|^2. \tag{2.87}$$

The first term is the stretching energy, which makes the wrinkles to take the excess wavelength because its prefactor is the largest. The second term penalizes departures from the uniaxial wavelength $\lambda_0 = (B/K)^{1/4}$ (Eq. (2.6)), where K is the substrate stiffness. The prefactor contains $\sigma = \sqrt{BK}$, the residual stress in presence of wrinkles, and the local excess length $\epsilon = a^2 k^2$. The last term penalizes the change in the wavevector, in particular the change in the orientation of the wrinkles. For simplicity, some terms have been simplified with respect to the expression given by Aharoni et al. [2017].

Making an analogy with the theory of smectic crystals, the authors argue that the width of a wall between domains with different wrinkle orientation is given by the ratio between the moduli of the two last terms:

$$\frac{\lambda_{\mathrm{w}}}{\lambda_0} \sim \sqrt{\frac{Y\epsilon}{\sigma}} \sim \frac{a}{t}. \tag{2.88}$$

However, this width is only observed for thick enough sheets, while thinner sheets develop conical singularities between domains [Chen and Hutchinson, 2004].

Simple geometric rules for wrinkle patterns. Tobasco et al. [2022] have analyzed the wrinkle patterns emerging when shells with different shapes cut out of surfaces with positive or negative Gauss curvature are placed on a liquid bath. They found that the resulting shape solves a maximum coverage problem, which is a geometric problem. Surprisingly, this analysis holds in the absence of surface tension pulling at the boundary of the shells, the residual stress playing the same role (Eq. (2.8)). They could then show that this geometric problem can be phrased in terms of simple geometric construction rules for the "stress carying lines", allowing them to predict the orientation of the wrinkles in complex shapes, and to identify disordered regions.

An important point in their analysis is the fact that the stress σ, or more precisely the "locking stress", which is a Lagrange multiplier, has a rank that is 1 or 0, meaning that it can be written

$$\sigma_{ij} = \lambda t_i t_j, \tag{2.89}$$

where $\lambda > 0$ is a scalar and $\boldsymbol{t}$ is a unit vector. We note that applying force balance to this expression yields

$$0 = \partial_i \sigma_{ij} = \partial_i(\lambda t_i) t_j + \lambda t_i \partial_i t_j. \tag{2.90}$$

Multiplying by t_j, the second term vanishes and we get

$$\partial_i(\lambda t_i) = 0. \tag{2.91}$$

We deduce that the second term in Eq. (2.90) has to vanish:

$$\lambda t_i \partial_i t_j = 0. \tag{2.92}$$

This means that either $\lambda = 0$, in which case the stress is zero and the orientation $\boldsymbol{t}$ is ill-defined, or $t_i \partial_i t_j = 0$, meaning that the "stress carying lines", the lines tangent to $\boldsymbol{t}$, are straight lines.

Chapter 3

Stress focusing

The preference of plates for isometric deformations may lead to the focalisation of deformations in small places. This is clearly visible in a crumpled paper sheet: most of the sheet is undeformed isometrically, while the deformation is large in some places, leaving "scars" that are observables when the sheet is unfolded [Plouraboué and Roux, 1996, Blair and Kudrolli, 2005]. Looking carefully at a crumpled sheet, one notices that these singularities may be points or ridges. These two types of singularities correspond to the developable cone, or *d-cone*, and the *stretching ridge* [Witten, 2007]. When studying these singularities, one usually wants to describe their morphology as well as their mechanical response. In this chapter, we discuss the parametrization and basic properties of these morphologies.

From these minimal singularities, there are still many obstacles to obtain the properties of a crumpled paper ball, such as friction, self-avoidance, and plasticity. To overcome these difficulties, many works have tried to describe crumpled paper with a top-down approach, trying to describe the experimental observations with minimal models [Deboeuf et al., 2013, Lahini et al., 2017, 2023, Shohat et al., 2023]. Some work has also been devoted to the study of the statistical properties of crumpled paper, such as the local ordering [Cambou and Menon, 2011, 2015] or the roughness of the uncrumpled surface [Plouraboué and Roux, 1996, Blair and Kudrolli, 2005]. These works are briefly discussed in this chapter.

We conclude this chapter by the discussion of "crumples", stress focusing features that appear beyond curved wrinkles in thin sheets King et al. [2012], Timounay et al. [2020].

3.1 Conical singularity

The conical singularity, has first been studied theoretically by Ben Amar and Pomeau [1997]. Such shape can easily be obtained experimentally by pushing a sheet through a cylinder with a point force [Chaïeb et al., 1998, Cerda and Mahadevan, 1998].

3.1.1 Geometry

In order to describe a conical configuration of the sheet, we choose the polar material coordinates centered at the tip of the cone, where the sheet takes the form [Witten, 2007]

$$\boldsymbol{R}(r, \theta) = r\hat{\boldsymbol{u}}(\theta), \tag{3.1}$$

where $\hat{\boldsymbol{u}}(\theta)$ is a unit vector. The conical shape is completely characterized by its intersection with the unit sphere centered at the tip of the cone, which is given by $\hat{\boldsymbol{u}}(\theta)$.

Provided that $|\hat{\boldsymbol{u}}'(\theta)| = 1$, this configuration is isometric to the planar reference shape. Notably, the Gauss curvature is zero since the sheet is flat in the r-direction, hence the surface is developpable; for this reason, this ideal shape is called the developpable-cone, or just "d-cone". This shape is singular ar $r = 0$, where the curvature diverges.

In order to get the bending energy, we have to compute the curvature of the sheet at (r, θ) in the θ-direction. Since $\hat{\boldsymbol{u}}(\theta)$ and $\hat{\boldsymbol{u}}'(\theta)$ are orthogonal unit vectors, the normal to the sheet is

$$\hat{\boldsymbol{n}}(\theta) = \hat{\boldsymbol{u}}(\theta) \times \hat{\boldsymbol{u}}'(\theta). \tag{3.2}$$

We note that $\hat{\boldsymbol{u}}(\theta) = \partial_r \boldsymbol{R}(r, \theta)$ and $\hat{\boldsymbol{u}}'(\theta) = r^{-1}\partial_\theta \boldsymbol{R}(r, \theta)$. The curvature in the direction θ is given by

$$c(r, \theta) = \hat{\boldsymbol{n}}(\theta) \cdot r^{-2}\partial_\theta^2 \boldsymbol{R}(r, \theta) = \frac{1}{r}\left[\hat{\boldsymbol{u}}(\theta) \times \hat{\boldsymbol{u}}'(\theta)\right] \cdot \boldsymbol{u}''(\theta) = \frac{\tilde{c}(\theta)}{r}, \tag{3.3}$$

where we have introduced the rescaled curvature $\tilde{c}(\theta)$.

We can parametrize $\hat{\boldsymbol{u}}(\theta)$ in spherical coordinates:

$$\hat{\boldsymbol{u}} = \begin{pmatrix} \cos(\phi)\sin(\beta) \\ \sin(\phi)\sin(\beta) \\ \cos(\beta) \end{pmatrix}, \tag{3.4}$$

where β and ϕ are functions of θ. We can compute

$$\hat{\boldsymbol{u}}' = \phi'\begin{pmatrix} -\sin(\phi)\sin(\beta) \\ \cos(\phi)\sin(\beta) \\ 0 \end{pmatrix} + \beta'\begin{pmatrix} \cos(\phi)\cos(\beta) \\ \sin(\phi)\cos(\beta) \\ -\sin(\beta) \end{pmatrix}. \tag{3.5}$$

Notably, the condition $|\hat{\boldsymbol{u}}'| = 1$ reads

$$|\hat{\boldsymbol{u}}'|^2 = \phi'^2\sin(\beta)^2 + \beta'^2 = 1. \tag{3.6}$$

To get simpler and more intuitive expressions, we consider a cone with a small slope: $\beta = \frac{\pi}{2} - \alpha$, with $|\alpha| \ll 1$. We start by rephrasing the isometry condition (3.6). At order α^0, it gives $\phi' = 1$, meaning that $\phi(\theta) = \theta$. We can parametrize the cone using the space coordinate ϕ instead of the material coordinate θ; now the isometry condition is global:

$$2\pi = \int_0^{2\pi}\left[\phi'^2\sin(\beta)^2 + \beta'^2\right]^{1/2}\mathrm{d}\theta = \int_0^{2\pi}\left[\sin(\beta)^2 + \left(\frac{\mathrm{d}\beta}{\mathrm{d}\phi}\right)^2\right]^{1/2}\mathrm{d}\phi \tag{3.7}$$

At order α^2, this relation becomes

$$\int_0^{2\pi}\left[\alpha'(\theta)^2 - \alpha(\theta)^2\right]\mathrm{d}\theta = 0. \tag{3.8}$$

Now the cone is completely defined by the function $\alpha(\phi)$ (the function $\phi(\theta)$ is only a reparametrisation of the unit circle of the original sheet).

We can then compute the curvature as a function of α. At order α, using $\phi = \theta$, we have

$$\hat{\boldsymbol{u}} = \begin{pmatrix} \cos(\theta) \\ \sin(\theta) \\ \alpha \end{pmatrix}, \tag{3.9}$$

$$\hat{\boldsymbol{u}}' = \begin{pmatrix} -\sin(\theta) \\ \cos(\theta) \\ 0 \end{pmatrix} + \alpha' \begin{pmatrix} 0 \\ 0 \\ 1 \end{pmatrix}, \tag{3.10}$$

$$\hat{\boldsymbol{n}} = \hat{\boldsymbol{u}} \times \hat{\boldsymbol{u}}' = \begin{pmatrix} -\alpha\cos(\theta) \\ -\alpha\sin(\theta) \\ 1 \end{pmatrix} + \alpha' \begin{pmatrix} \sin(\theta) \\ -\cos(\theta) \\ 0 \end{pmatrix}, \tag{3.11}$$

$$\boldsymbol{u}'' = -\begin{pmatrix} \cos(\theta) \\ \sin(\theta) \\ 0 \end{pmatrix} + \alpha'' \begin{pmatrix} 0 \\ 0 \\ 1 \end{pmatrix}. \tag{3.12}$$

So that the curvature is

$$\tilde{c}(\theta) = \hat{\boldsymbol{n}} \cdot \boldsymbol{u}'' = \alpha'' + \alpha. \tag{3.13}$$

3.1.2 Mechanics

The bending energy of an annular plate $R_c < r < R$ is given by

$$U_{\text{bend}} = \frac{B}{2} \int_{R_{\text{core}}}^{R} r \mathrm{d}r \int_0^{2\pi} \mathrm{d}\theta c(r,\theta)^2 = \frac{B}{2} \log\left(\frac{R}{R_{\text{core}}}\right) \int_0^{2\pi} \tilde{c}(\theta)^2 \mathrm{d}\theta. \tag{3.14}$$

The singularity at the tip of the cone appears in the divergence of the bending energy as $R_{\text{core}} \to 0$. In the limit of small slope, the bending energy thus reads

$$U_{\text{bend}} = \frac{B}{2} \log\left(\frac{R}{R_{\text{core}}}\right) \int_0^{2\pi} \left[\alpha''(\theta) + \alpha(\theta)\right]^2 \mathrm{d}\theta. \tag{3.15}$$

When a sheet is pushed through a cylinder, a geometrical constraint $\alpha \geq \alpha_0$ is imposed, where α_0 is given by the radius of the cylinder and the indentation depth. To find the shape of the cone, $\alpha(\theta)$, we should minimize the energy (3.15) under the isometry constraint (3.8) and the constraint $\alpha \geq \alpha_0$ (otherwise $\alpha = 0$ would be a solution). This problem resembles Euler buckling, and is also similar to the formation of a ruck in a rug [Vella et al., 2009, Kolinski et al., 2009]. Solving the equations, one gets the angular size of the region that looses contact with the cylinder: $\Delta\theta \simeq 139°$ [Audoly and Pomeau, 2010].

3.1.3 Size of the core

For $r < R_c$, the diverging bending energy is regularized by allowing some stretching. We look for R_c with scaling arguments. The curvature in the isometric region is of order $\tilde{c} \sim \alpha_0$, leading to a bending energy

$$U_{\text{bend}} \sim B\alpha_0^2 \log\left(\frac{R}{R_{\text{core}}}\right). \tag{3.16}$$

The radius of curvature of the core is $R_{\text{curv}} \sim R_{\text{core}}/\alpha_0$, hence its Gauss curvature is $\kappa_G \sim (\alpha_0/R_{\text{core}})^2$, generating a strain $\epsilon \sim \kappa_G R_{\text{core}}^2 \sim \alpha_0^2$ from Eq. (1.58). The stretching energy is thus

$$U_{\text{str}} \sim YR_{\text{core}}^2 \epsilon^2 \sim YR_{\text{core}}^2 \alpha_0^2. \tag{3.17}$$

Balancing the bending and stretching energies, we find the optimal value

$$R_{\text{core}} \sim \sqrt{\frac{B}{Y}} \sim t : \tag{3.18}$$

the size of the core should be given by the thickness of the material [Witten, 2007]. The corresponding energy is

$$\boxed{U_{\text{cone}} \sim B\alpha_0^2 \log(R/t).} \tag{3.19}$$

However, the core is much larger in the experiments; it also has a crescent shape, which to date is not completely understood.

3.2   Ridge singularity

A ridge appears for instance between two developpable-cones. We denote W the width of the ridge (the distance between the centers of the cones). On the sides of the ridge, a sharp angle α is imposed of the sheet. Having a sharp angle along the ridge would cost an infinite bending energy, so that there should be a finite curvature radius along the ridge, say $R(s)$, that goes to 0 as $s \rightarrow 0$ or $s \rightarrow W$. This ridge, which should appear during crumpling, has been studied by Lobkovsky et al. [1995].

We provide a scaling argument for the curvature radius. We just need the maximal curvature radius, $R(W/2) = R$. The bending energy per unit area is

$$U_{\text{bend}} \sim \frac{B}{R^2}. \tag{3.20}$$

The finite radius of curvature generates a stretching ϵ along the ridge, associated to a stretching energy density $U_{\text{str}} \sim Y\epsilon^2$. In order to evaluate ϵ, we consider the maximal deviation ζ of the ridge from a straight line. From geometric arguments we get $\zeta \sim \alpha^2 R$. The stretching of the ridge is $\epsilon \sim (\zeta/W)^2 \sim (\alpha^2 R/W)^2$. The stretching energy density is thus

$$U_{\text{str}} \sim Y \left(\frac{\alpha^2 R}{W} \right)^4. \tag{3.21}$$

Balancing the stretching and bending energies, we find

$$R \sim t^{1/3} W^{2/3} \alpha^{-4/3}. \tag{3.22}$$

The deformation cover an area $W \times \alpha R$, so that the energy of this ridge is

$$\boxed{U_{\text{ridge}} \sim Y t^{5/3} W^{1/3} \alpha^{7/3}.} \tag{3.23}$$

We should note the peculiar scaling of the ridge; one would naively expect a dependence on W and α as $U \sim \alpha^2 W$.

The scaling analysis presented here can be made rigorous by solving the Föppl-von Kármán equations. In this case the scaling results can be derived by a proper rescaling of the equations [Lobkovsky and Witten, 1997].

We compare the energies of cones and ridges. The energy of a ridge (3.23) can be written as $U_{\text{ridge}} \sim B(W/t)^{1/3}\alpha^{7/3}$. For $x = W/t \gg 1$, $x^{1/3} \gg \log(x)$, hence the energy of the ridges should be dominant in a crumpled state.

Stretched and twisted ribbons. Ridges that ressemble stretching ridges have been reported in stretched and twisted ribbons [Pham Dinh et al., 2016, Chopin and Kudrolli, 2016].

3.3 Experimental and numerical studies

The sheet can be followed in 3D optically during the early stage of crumpling [Aharoni and Sharon, 2010]. At the late stage, the shape can be obtained via X-ray microtomography [Cambou and Menon, 2011]. One can look for instance to the sheet orientation as a function of its position in the crumpled ball, or at the number of contacts, getting information about the role of friction. Another (cheaper) way to get information about the structure is to cut through the crumpled ball [Sultan and Boudaoud, 2006, Deboeuf et al., 2013]. In order to reduce the effect of friction, one can use a fluid in order to lubricate the contacts [Cambou and Menon, 2015].

However, it is not straightforward to reconstruct the shape in material coordinates from the tomography data or from a cut. The properties of the network of ridges may be obtained by analysing the unfolded sheet, plasticity keeping track of the ridges [Blair and Kudrolli, 2005, Sultan and Boudaoud, 2006, Andresen et al., 2007]. From the distribution of ridges length, one can infer that crumpling is hierarchical: long ridges form first, then they break in smaller ridges, and so on, analogously to what happens in repeated folding [Deboeuf et al., 2013]. Moreover, the ridges are not always static, as the conical singularities can move [Aharoni and Sharon, 2010], leaving behind them plastically deformed furrows [Gottesman et al., 2015].

The mechanical response can be obtained by placing the crumpled ball in a cylinder with a weighted piston on it and looking at the displacement of the piston as a function of time (this is a much simpler geometry than a confining sphere with a decreasing radius). Due to the interplay of the hierarchical structure and friction effects, the dynamics may be logarithmic [Matan et al., 2002]: the displacement $h(t)$ follows $h(t) = A \log(t)$ for several decades in time. This dependence is not yet understood. The mechanics can be related to the properties of the sound emitted during crumpling, which is easy to measure [Kramer and Lobkovsky, 1996, Houle and Sethna, 1996].

Finally, numerical simulations allow to choose the ingredients to take into account. For instance, one can simulate the crumpling of non-self-avoiding ("phantom") sheets [Vliegenthart and Gompper, 2006], or tune the effects of plasticity [Tallinen et al., 2009].

3.4 From wrinkles to "crumples"

Bent wrinkles may give way to "crumples", diamond-like stress focusing structures. This transition has been reported for the first time for the sheet on drop experiment [King et al., 2012], but it has been shown to arise in a variety of settings: an indented sheet, a uniaxially compressed sheet on a curved interface, a pressurized balloon [Timounay et al., 2020].

Timounay et al. [2020] have shown that the transition involves the length ℓ of the wrinkles, their radius of curvature R, their tension σ and the stretching modulus of the sheet Y. They have shown that, in all their settings, crumples are observed for

$$\left(\frac{\ell}{R}\right)^2 \gtrsim 300\frac{\sigma}{Y}, \tag{3.24}$$

the factor 300 being empirical. Moreover, they have shown exhibited specific patterns of origami bellows [Reid et al., 2017] that ressemble crumples.

Despite these hints, the crumples still lack a consistent model that would allow to predict their features and the threshold (3.24).

Bibliography

Hillel Aharoni and Eran Sharon. Direct observation of the temporal and spatial dynamics during crumpling. *Nat Mater*, 9(12):993–997, 12 2010. ISSN 1476-1122. URL http://dx.doi.org/10.1038/nmat2893. 10.1038/nmat2893.

Hillel Aharoni, Desislava V. Todorova, Octavio Albarrán, Lucas Goehring, Randall D. Kamien, and Eleni Katifori. The smectic order of wrinkles. *Nature Communications*, 8(1):15809, 2017. ISSN 2041-1723. doi: 10.1038/ncomms15809. URL https://doi.org/10.1038/ncomms15809.

Hillel Aharoni, Yu Xia, Xinyue Zhang, Randall D. Kamien, and Shu Yang. Universal inverse design of surfaces with thin nematic elastomer sheets. *Proceedings of the National Academy of Sciences*, 115(28):7206–7211, 2018. doi: 10.1073/pnas.1804702115. URL https://www.pnas.org/doi/abs/10.1073/pnas.1804702115.

Christian André Andresen, Alex Hansen, and Jean Schmittbuhl. Ridge network in crumpled paper. *Phys. Rev. E*, 76(2):026108, Aug 2007. doi: 10.1103/PhysRevE.76.026108. URL http://link.aps.org/doi/10.1103/PhysRevE.76.026108.

Shahaf Armon, Efi Efrati, Raz Kupferman, and Eran Sharon. Geometry and Mechanics in the Opening of Chiral Seed Pods. *Science*, 333(6050):1726–1730, 2011. doi: 10.1126/science.1203874. URL http://www.sciencemag.org/content/333/6050/1726.abstract.

B. Audoly. Localized buckling of a floating elastica. *Phys. Rev. E*, 84(1):011605, Jul 2011. doi: 10.1103/PhysRevE.84.011605. URL https://link.aps.org/doi/10.1103/PhysRevE.84.011605.

B. Audoly and Y. Pomeau. *Elasticity and geometry: from hair curls to the non-linear response of shells*. Oxford University Press Oxford, 2010.

M. Ben Amar and Y. Pomeau. Crumpled paper. *Proc. Royal Soc. A*, 453(1959):729–755, 1997. doi: 10.1098/rspa.1997.0041. URL http://rspa.royalsocietypublishing.org/content/453/1959/729.abstract.

H. Bense, M. Tani, M. Saint-Jean, E. Reyssat, B. Roman, and J. Bico. Elastocapillary adhesion of a soft cap on a rigid sphere. *Soft Matter*, 2020. doi: 10.1039/C9SM02057H. URL http://dx.doi.org/10.1039/C9SM02057H.

Daniel L. Blair and Arshad Kudrolli. Geometry of Crumpled Paper. *Phys. Rev. Lett.*, 94(16):166107, Apr 2005. doi: 10.1103/PhysRevLett.94.166107. URL http://link.aps.org/doi/10.1103/PhysRevLett.94.166107.

Finn Box, Lucie Domino, Tiago Outerelo Corvo, Mokhtar Adda-Bedia, Vincent Démery, Dominic Vella, and Benny Davidovitch. Delamination from an adhesive sphere: Curvature-induced dewetting versus buckling. *Proc. Natl. Acad. Sci.*, 120(12):e2212290120, 2023. doi: 10.1073/pnas.2212290120. URL https://www.pnas.org/doi/abs/10.1073/pnas.2212290120.

Fabian Brau, Hugues Vandeparre, Abbas Sabbah, Christophe Poulard, Arezki Boudaoud, and Pascal Damman. Multiple-length-scale elastic instability mimics parametric resonance of nonlinear oscillators. *Nat Phys*, 7(1):56–60, 01 2011. ISSN 1745-2473. URL http://dx.doi.org/10.1038/nphys1806. 10.1038/nphys1806.

Anne Dominique Cambou and Narayanan Menon. Three-dimensional structure of a sheet crumpled into a ball. *Proceedings of the National Academy of Sciences*, 108(36):14741–14745, 2011. doi: 10.1073/pnas. 1019192108. URL http://www.pnas.org/content/108/36/14741.abstract.

Anne Dominique Cambou and Narayanan Menon. Orientational ordering in crumpled elastic sheets. *EPL*, 112(1):14003, 2015. doi: 10.1209/0295-5075/112/14003. URL http://dx.doi.org/10.1209/0295-5075/112/14003.

E. Cerda and L. Mahadevan. Conical Surfaces and Crescent Singularities in Crumpled Sheets. *Phys. Rev. Lett.*, 80(11):2358–2361, Mar 1998. doi: 10.1103/PhysRevLett.80.2358. URL http://link.aps.org/doi/10.1103/PhysRevLett.80.2358.

E. Cerda and L. Mahadevan. Geometry and Physics of Wrinkling. *Phys. Rev. Lett.*, 90(7):074302, Feb 2003. doi: 10.1103/PhysRevLett.90.074302. URL http://link.aps.org/doi/10.1103/PhysRevLett.90.074302.

Sahraoui Chaïeb, Francisco Melo, and Jean-Christophe Géminard. Experimental Study of Developable Cones. *Phys. Rev. Lett.*, 80(11):2354–2357, Mar 1998. doi: 10.1103/PhysRevLett.80.2354. URL http://link.aps.org/doi/10.1103/PhysRevLett.80.2354.

X. Chen and John W. Hutchinson. Herringbone Buckling Patterns of Compressed Thin Films on Compliant Substrates . *Journal of Applied Mechanics*, 71(5):597–603, 11 2004. ISSN 0021-8936. doi: 10.1115/1.1756141. URL https://doi.org/10.1115/1.1756141.

Julien Chopin and Arshad Kudrolli. Disclinations, e-cones, and their interactions in extensible sheets. *Soft Matter*, 12(19):4457–4462, 2016. doi: 10.1039/C6SM00187D. URL http://dx.doi.org/10.1039/C6SM00187D.

Julien Chopin, Vincent Démery, and Benny Davidovitch. Roadmap to the morphological instabilities of a stretched twisted ribbon. *J. Elast.*, 119(1):137–189, 2015. ISSN 1573-2681. doi: 10.1007/s10659-014-9498-x. URL https://doi.org/10.1007/s10659-014-9498-x.

Benny Davidovitch and Vincent Démery. Rucks and folds: delamination from a flat rigid substrate under uniaxial compression. *Eur. Phys. J. E*, 44(2):11, 2021. doi: 10.1140/epje/s10189-021-00020-1. URL https://doi.org/10.1140/epje/s10189-021-00020-1.

Benny Davidovitch, Robert D. Schroll, Dominic Vella, Mokhtar Adda-Bedia, and Enrique A. Cerda. Prototypical model for tensional wrinkling in thin sheets. *Proceedings of the National Academy of Sciences*, 108(45):18227–18232, 2011. doi: 10.1073/pnas.1108553108. URL http://www.pnas.org/content/108/45/18227.abstract.

Benny Davidovitch, Yiwei Sun, and Gregory M. Grason. Geometrically incompatible confinement of solids. *Proceedings of the National Academy of Sciences*, 116(5):1483–1488, 2019. ISSN 0027-8424. doi: 10.1073/pnas.1815507116. URL https://www.pnas.org/content/116/5/1483.

S. Deboeuf, E. Katzav, A. Boudaoud, D. Bonn, and M. Adda-Bedia. Comparative Study of Crumpling and Folding of Thin Sheets. *Phys. Rev. Lett.*, 110(10):104301, Mar 2013. doi: 10.1103/PhysRevLett.110.104301. URL http://link.aps.org/doi/10.1103/PhysRevLett.110.104301.

Haim Diamant and Thomas A. Witten. Compression Induced Folding of a Sheet: An Integrable System. *Phys. Rev. Lett.*, 107(16):164302, Oct 2011. doi: 10.1103/PhysRevLett.107.164302. URL http://link.aps.org/doi/10.1103/PhysRevLett.107.164302.

M. A. Dias, J. A. Hanna, and C. D. Santangelo. Programmed buckling by controlled lateral swelling in a thin elastic sheet. *Phys. Rev. E*, 84(3):036603, Sep 2011. doi: 10.1103/PhysRevE.84.036603. URL http://link.aps.org/doi/10.1103/PhysRevE.84.036603.

Vincent Démery, Benny Davidovitch, and Christian D. Santangelo. Mechanics of large folds in thin interfacial films. *Phys. Rev. E*, 90(4):042401, Oct 2014. doi: 10.1103/PhysRevE.90.042401. URL http://link.aps.org/doi/10.1103/PhysRevE.90.042401.

Omer Gottesman, Efi Efrati, and Shmuel M. Rubinstein. Furrows in the wake of propagating d-cones. *Nature Communications*, 6:7232 EP –, 06 2015. URL http://dx.doi.org/10.1038/ncomms8232. Article.

Itay Griniasty, Hillel Aharoni, and Efi Efrati. Curved geometries from planar director fields: Solving the two-dimensional inverse problem. *Phys. Rev. Lett.*, 123:127801, Sep 2019. doi: 10.1103/PhysRevLett.123.127801. URL https://link.aps.org/doi/10.1103/PhysRevLett.123.127801.

J. C. Géminard, R. Bernal, and F. Melo. Wrinkle formations in axi-symmetrically stretched membranes. *The European Physical Journal E*, 15(2):117–126, 2004. ISSN 1292-895X. doi: 10.1140/epje/i2004-10041-1. URL http://dx.doi.org/10.1140/epje/i2004-10041-1.

Mengfei He, Vincent Démery, and Joseph D. Paulsen. Cross-sections of doubly curved sheets as confined elastica. *Proceedings of the National Academy of Sciences*, 120(11):e2216786120, 2023. doi: 10.1073/pnas.2216786120. URL https://www.pnas.org/doi/abs/10.1073/pnas.2216786120.

Paul A. Houle and James P. Sethna. Acoustic emission from crumpling paper. *Phys. Rev. E*, 54(1):278–283, Jul 1996. doi: 10.1103/PhysRevE.54.278. URL http://link.aps.org/doi/10.1103/PhysRevE.54.278.

Jiangshui Huang, Megan Juszkiewicz, Wim H. de Jeu, Enrique Cerda, Todd Emrick, Narayanan Menon, and Thomas P. Russell. Capillary Wrinkling of Floating Thin Polymer Films. *Science*, 317(5838):650–653, 2007. doi: 10.1126/science.1144616. URL http://www.sciencemag.org/content/317/5838/650.abstract.

Jiangshui Huang, Benny Davidovitch, Christian D. Santangelo, Thomas P. Russell, and Narayanan Menon. Smooth Cascade of Wrinkles at the Edge of a Floating Elastic Film. *Phys. Rev. Lett.*, 105(3):038302, Jul 2010. doi: 10.1103/PhysRevLett.105.038302. URL http://link.aps.org/doi/10.1103/PhysRevLett.105.038302.

Jérémy Hure, Benoît Roman, and José Bico. Wrapping an Adhesive Sphere with an Elastic Sheet. *Phys. Rev. Lett.*, 106(17):174301, Apr 2011. doi: 10.1103/PhysRevLett.106.174301. URL https://link.aps.org/doi/10.1103/PhysRevLett.106.174301.

Jungwook Kim, James A. Hanna, Myunghwan Byun, Christian D. Santangelo, and Ryan C. Hayward. Designing Responsive Buckled Surfaces by Halftone Gel Lithography. *Science*, 335(6073):1201–1205, 2012. doi: 10.1126/science.1215309. URL http://www.sciencemag.org/content/335/6073/1201.abstract.

H. King, R. D. Schroll, B. Davidovitch, and N. Menon. Elastic sheet on a liquid drop reveals wrinkling and crumpling as distinct symmetry-breaking instabilities. *Proc. Natl. Acad. Sci. U.S.A.*, 109(25):9716–9720, 2012. doi: 10.1073/pnas.1201201109.

Yael Klein, Efi Efrati, and Eran Sharon. Shaping of Elastic Sheets by Prescription of Non-Euclidean Metrics. *Science*, 315(5815):1116–1120, 2007. doi: 10.1126/science.1135994. URL http://www.sciencemag.org/content/315/5815/1116.abstract.

John M. Kolinski, Pascale Aussillous, and L. Mahadevan. Shape and Motion of a Ruck in a Rug. *Phys. Rev. Lett.*, 103(17):174302, Oct 2009. doi: 10.1103/PhysRevLett.103.174302. URL http://link.aps.org/doi/10.1103/PhysRevLett.103.174302.

Eric M. Kramer and Alexander E. Lobkovsky. Universal power law in the noise from a crumpled elastic sheet. *Phys. Rev. E*, 53(2):1465–1469, Feb 1996. doi: 10.1103/PhysRevE.53.1465. URL http://link.aps.org/doi/10.1103/PhysRevE.53.1465.

Yoav Lahini, Omer Gottesman, Ariel Amir, and Shmuel M. Rubinstein. Nonmonotonic Aging and Memory Retention in Disordered Mechanical Systems. *Phys. Rev. Lett.*, 118(8):085501, Feb 2017. doi: 10.1103/PhysRevLett.118.085501. URL https://link.aps.org/doi/10.1103/PhysRevLett.118.085501.

Yoav Lahini, Shmuel M. Rubinstein, and Ariel Amir. Crackling noise during slow relaxations in crumpled sheets. *Phys. Rev. Lett.*, 130:258201, Jun 2023. doi: 10.1103/PhysRevLett.130.258201. URL https://link.aps.org/doi/10.1103/PhysRevLett.130.258201.

Alex Lobkovsky, Sharon Gentges, Hao Li, David Morse, and Thomas A. Witten. Scaling properties of stretching ridges in a crumpled elastic sheet. *SCIENCE-NEW YORK THEN WASHINGTON-*, pages 1482–1484, 1995.

Alexander E. Lobkovsky and T. A. Witten. Properties of ridges in elastic membranes. *Phys. Rev. E*, 55 (2):1577–1589, Feb 1997. doi: 10.1103/PhysRevE.55.1577. URL http://link.aps.org/doi/10.1103/PhysRevE.55.1577.

C. Majidi and R. S. Fearing. Adhesion of an elastic plate to a sphere. *Proceedings of the Royal Society A: Mathematical, Physical and Engineering Sciences*, 464(2093):1309–1317, 2008. doi: {10.1098/rspa.2007.0341}URL.

E. H. Mansfield. Tension field theory, a new approach which shows its duality with inextensional theory. In Miklós Hetényi and Walter G. Vincenti, editors, *Applied Mechanics*, pages 305–320, Berlin, Heidelberg, 1969. Springer Berlin Heidelberg. ISBN 978-3-642-85640-2.

M. Marder, E. Sharon, S. Smith, and B. Roman. Theory of edges of leaves. *Europhysics Letters (EPL)*, 62(4):498–504, may 2003. doi: 10.1209/epl/i2003-00334-5. URL https://doi.org/10.1209%2Fepl%2Fi2003-00334-5.

Kittiwit Matan, Rachel B. Williams, Thomas A. Witten, and Sidney R. Nagel. Crumpling a Thin Sheet. *Phys. Rev. Lett.*, 88(7):076101, Jan 2002. doi: 10.1103/PhysRevLett.88.076101. URL http://link.aps.org/doi/10.1103/PhysRevLett.88.076101.

J. D. Paulsen, V. Démery, C. D. Santangelo, T. P. Russell, B. Davidovitch, and N. Menon. Optimal wrapping of liquid droplets with ultrathin sheets. *Nat Mater*, 14(12):1206–1209, 12 2015. ISSN 1476-1122. URL http://dx.doi.org/10.1038/nmat4397. Letter.

J. D. Paulsen, V. Démery, K. B. Toga, Z. Qiu, T. P. Russell, B. Davidovitch, and N. Menon. Geometry-Driven Folding of a Floating Annular Sheet. *Phys. Rev. Lett.*, 118(4):048004, Jan 2017. doi: 10.1103/PhysRevLett.118.048004. URL http://link.aps.org/doi/10.1103/PhysRevLett.118.048004.

Joseph D. Paulsen, Evan Hohlfeld, Hunter King, Jiangshui Huang, Zhanlong Qiu, Thomas P. Russell, Narayanan Menon, Dominic Vella, and Benny Davidovitch. Curvature-induced stiffness and the spatial

variation of wavelength in wrinkled sheets. *Proceedings of the National Academy of Sciences*, 113(5): 1144–1149, 2016. doi: 10.1073/pnas.1521520113. URL http://www.pnas.org/content/113/5/1144.abstract.

William H. Paulsen. What is the shape of a Mylar balloon? *American Mathematical Monthly*, pages 953–958, 1994.

H. Pham Dinh, V. Démery, B. Davidovitch, F. Brau, and P. Damman. From Cylindrical to Stretching Ridges and Wrinkles in Twisted Ribbons. *Phys. Rev. Lett.*, 117(10):104301, Sep 2016. doi: 10.1103/PhysRevLett.117.104301. URL http://link.aps.org/doi/10.1103/PhysRevLett.117.104301.

Miguel Piñeirua, Nana Tanaka, Benoit Roman, and Jose Bico. Capillary buckling of a floating annulus. *Soft Matter*, 9(46):10985–10992, 2013. doi: 10.1039/C3SM51825F. URL http://dx.doi.org/10.1039/C3SM51825F.

Franck Plouraboué and Stéphane Roux. Experimental study of the roughness of crumpled surfaces . *Physica A: Statistical Mechanics and its Applications* , 227(3–4):173–182, 1996. ISSN 0378-4371. doi: http://dx.doi.org/10.1016/0378-4371(95)00380-0. URL http://www.sciencedirect.com/science/article/pii/0378437195003800.

L. Pocivavsek, R. Dellsy, A. Kern, S. Johnson, B. Lin, K. Y. C. Lee, and E. Cerda. Stress and Fold Localization in Thin Elastic Membranes. *Science*, 320(5878):912–916, 2008. doi: 10.1126/science.1154069.

Charlotte Py, Paul Reverdy, Lionel Doppler, José Bico, Benoît Roman, and Charles N. Baroud. Capillary Origami: Spontaneous Wrapping of a Droplet with an Elastic Sheet. *Phys. Rev. Lett.*, 98(15):156103, Apr 2007. doi: 10.1103/PhysRevLett.98.156103. URL http://link.aps.org/doi/10.1103/PhysRevLett.98.156103.

Austin Reid, Frederic Lechenault, Sergio Rica, and Mokhtar Adda-Bedia. Geometry and design of origami bellows with tunable response. *Phys. Rev. E*, 95:013002, Jan 2017. doi: 10.1103/PhysRevE.95.013002. URL https://link.aps.org/doi/10.1103/PhysRevE.95.013002.

B. Roman and J. Bico. Elasto-capillarity: deforming an elastic structure with a liquid droplet. *Journal Of Physics-Condensed Matter*, 22(49):493101, 2010. doi: 10.1088/0953-8984/22/49/493101. URL http://stacks.iop.org/0953-8984/22/i=49/a=493101.

Zachariah S. Schrecengost, Seif Hejazine, Jordan V. Barrett, Vincent Démery, and Joseph D. Paulsen. Shape of a membrane on a liquid interface with arbitrary curvatures. *Phys. Rev. Lett.*, 134:188202, May 2025. doi: 10.1103/PhysRevLett.134.188202. URL https://link.aps.org/doi/10.1103/PhysRevLett.134.188202.

Eran Sharon and Efi Efrati. The mechanics of non-Euclidean plates. *Soft Matter*, 6(22):5693–5704, 2010. doi: 10.1039/C0SM00479K. URL http://dx.doi.org/10.1039/C0SM00479K.

Eran Sharon, Benoit Roman, Michael Marder, Gyu-Seung Shin, and Harry L. Swinney. Mechanics: Buckling cascades in free sheets. *Nature*, 419(6907):579–579, 10 2002. ISSN 0028-0836. URL http://dx.doi.org/10.1038/419579a. 10.1038/419579a.

Eran Sharon, Benoît Roman, and Harry L. Swinney. Geometrically driven wrinkling observed in free plastic sheets and leaves. *Phys. Rev. E*, 75(4):046211, Apr 2007. doi: 10.1103/PhysRevE.75.046211. URL https://link.aps.org/doi/10.1103/PhysRevE.75.046211.

Dor Shohat, Yaniv Friedman, and Yoav Lahini. Logarithmic aging via instability cascades in disordered systems. *Nature Physics*, 19(12):1890–1895, 2023. ISSN 1745-2481. doi: 10.1038/s41567-023-02220-2. URL https://doi.org/10.1038/s41567-023-02220-2.

Emmanuel Siéfert, Etienne Reyssat, José Bico, and Benoît Roman. Bio-inspired pneumatic shape-morphing elastomers. *Nature Materials*, 18(1):24–28, 2019. ISSN 1476-4660. URL https://doi.org/10.1038/s41563-018-0219-x.

Emmanuel Siéfert, Etienne Reyssat, José Bico, and Benoît Roman. Programming stiff inflatable shells from planar patterned fabrics. *Soft Matter*, 16:7898–7903, 2020. doi: 10.1039/D0SM01041C. URL http://dx.doi.org/10.1039/D0SM01041C.

Robert W. Style, Rostislav Boltyanskiy, Yonglu Che, J. S. Wettlaufer, Larry A. Wilen, and Eric R. Dufresne. Universal Deformation of Soft Substrates Near a Contact Line and the Direct Measurement of Solid Surface Stresses. *Phys. Rev. Lett.*, 110(6):066103, Feb 2013. doi: 10.1103/PhysRevLett.110.066103. URL http://link.aps.org/doi/10.1103/PhysRevLett.110.066103.

Eric Sultan and Arezki Boudaoud. Statistics of Crumpled Paper. *Phys. Rev. Lett.*, 96(13):136103, Apr 2006. doi: 10.1103/PhysRevLett.96.136103. URL http://link.aps.org/doi/10.1103/PhysRevLett.96.136103.

T. Tallinen, J. A. Astrom, and J. Timonen. The effect of plasticity in crumpling of thin sheets. *Nat Mater*, 8(1):25–29, 01 2009. ISSN 1476-1122. URL http://dx.doi.org/10.1038/nmat2343. 10.1038/nmat2343.

G Taylor. On the shape of parachutes. *Advisory Committee for Aeronautics*, 1919.

Yousra Timounay, Raj De, Jessica L. Stelzel, Zachariah S. Schrecengost, Monica M. Ripp, and Joseph D. Paulsen. Crumples as a Generic Stress-Focusing Instability in Confined Sheets. *Phys. Rev. X*, 10(2):021008, Apr 2020. doi: 10.1103/PhysRevX.10.021008. URL https://link.aps.org/doi/10.1103/PhysRevX.10.021008.

Yousra Timounay, Alexander R. Hartwell, Mengfei He, D. Eric King, Lindsay K. Murphy, Vincent Démery, and Joseph D. Paulsen. Sculpting liquids with ultrathin shells. *Phys. Rev. Lett.*, 127:108002, Sep 2021. doi: 10.1103/PhysRevLett.127.108002. URL https://link.aps.org/doi/10.1103/PhysRevLett.127.108002.

Ian Tobasco, Yousra Timounay, Desislava Todorova, Graham C. Leggat, Joseph D. Paulsen, and Eleni Katifori. Exact solutions for the wrinkle patterns of confined elastic shells. *Nature Physics*, August 2022. ISSN 1745-2481. URL https://doi.org/10.1038/s41567-022-01672-2.

Hugues Vandeparre, Miguel Piñeirua, Fabian Brau, Benoit Roman, José Bico, Cyprien Gay, Wenzhong Bao, Chun Ning Lau, Pedro M. Reis, and Pascal Damman. Wrinkling Hierarchy in Constrained Thin Sheets from Suspended Graphene to Curtains. *Phys. Rev. Lett.*, 106(22):224301, Jun 2011. doi: 10.1103/PhysRevLett.106.224301. URL http://link.aps.org/doi/10.1103/PhysRevLett.106.224301.

D. Vella, P. Aussillous, and L. Mahadevan. Elasticity of an interfacial particle raft. *EPL (Europhysics Letters)*, 68(2):212, 2004. URL http://stacks.iop.org/0295-5075/68/i=2/a=212.

Dominic Vella, Arezki Boudaoud, and Mokhtar Adda-Bedia. Statics and Inertial Dynamics of a Ruck in a Rug. *Phys. Rev. Lett.*, 103(17):174301, Oct 2009. doi: 10.1103/PhysRevLett.103.174301. URL http://link.aps.org/doi/10.1103/PhysRevLett.103.174301.

Dominic Vella, Amin Ajdari, Ashkan Vaziri, and Arezki Boudaoud. Wrinkling of Pressurized Elastic Shells. *Phys. Rev. Lett.*, 107(17):174301, Oct 2011. doi: 10.1103/PhysRevLett.107.174301. URL https://link.aps.org/doi/10.1103/PhysRevLett.107.174301.

G. A. Vliegenthart and G. Gompper. Forced crumpling of self-avoiding elastic sheets. *Nat Mater*, 5(3):216–221, 03 2006. ISSN 1476-1122. URL http://dx.doi.org/10.1038/nmat1581. 10.1038/nmat1581.

T. A. Witten. Stress focusing in elastic sheets. *Rev. Mod. Phys.*, 79(2):643–675, Apr 2007. doi: 10.1103/RevModPhys.79.643. URL http://link.aps.org/doi/10.1103/RevModPhys.79.643.